

國立臺灣大學理學院地質科學研究所

碩士論文

Department of Geosciences,

College of Science

National Taiwan University

Master Thesis



時間相依走時層析成像反演之探討：
以 2013 年瑞穗地震(M_L 6.4)為例

Investigating the uncertainty of time-dependent
seismic velocity changes using travel time tomography: a
case study of the M_L 6.4 2013 Rueisuei earthquake,
Taiwan

馮冠芙

Kuan-Fu Feng

指導教授：吳逸民 博士

Advisor: Yih-Min Wu, Ph.D.

中華民國 105 年 6 月

June, 2016



國立臺灣大學碩士學位論文 口試委員會審定書

時間相依走時層析成像反演之探討：
以 2013 年瑞穗地震(M_L 6.4)為例

Investigating the uncertainty of time-dependent
seismic velocity changes using travel time tomography: a
case study of the M_L 6.4 2013 Rueisuei earthquake,
Taiwan

本論文係 馮冠笑 君 (學號 R03224202) 在國立臺灣大學
地質科學研究所完成之碩士學位論文，於民國 105 年 6 月 23
日承下列考試委員審查通過及口試及格，特此證明

口試委員

吳逸民
(指導教授)

趙里

李憲忠

郭陳濤

趙里

李憲忠

郭陳濤

誌謝



兩年的碩士班生涯很快地接近尾聲，回首彷彿昨日歷歷在目，希望一路走來所有遇到的挫折、困難，讓我在這段期間內有所成長。

首先要感謝指導教授 吳逸民老師，自我尚未進入臺大時即給予生活上以及研究上的許多幫助，在就讀研究所期間給予極大的自由度和學術上的支持與資源，讓我比其他人擁有更多機會，平時更透過無數的對談分享經驗，學生受益良多，在此致上最誠摯的感謝。這本論文能夠完整，要感謝口試委員 趙里老師、李憲忠老師、郭陳浩老師給予寶貴的意見與建議，經過老師們審視，讓這本論文更加完備，於此學生由衷感恩。

在研究路上要特別感謝 炫哥、vvn、信業耐心地指導，在和你們討論的過程中體悟到學術論證的嚴謹態度，並總能從你們眼中看見面對研究時那閃閃發亮的眼神。謝謝 311 的各位助理們、學長姊、學弟妹，特別是喬姊在行政上一直以來的幫助，很開心能夠成為 Seismolab 歡樂大家庭的一員。除此之外，當然還有 316 的琬鈴、地質所水輝學長、睿明學長和同學們，以及所有幫助我、關心我的各位，謝謝你們在我煎熬難過時給予的各種鼓勵與陪伴。

在此容我一提，回顧求學生涯，要特別感謝中正大學 歐國斌老師在我大學在學期間給予的鼓勵和自我價值的肯定，對我意義非凡，學生由衷感謝。


最後，將本論文獻給我摯愛的家人、親友，謝謝你們的陪伴、支持與包容，讓我無後顧之憂地完成碩士學位。

中文摘要



中-大型地震前後地殼速度變化可以透過地震波走時層析成像法解析，然而，兩個時期不相等的震源-測站之波線路徑在空間中的分佈會使層析成像的速度變化結果產生偏差。為了測試由於地震波線分佈不相等對於解析速度構造變化造成的偏差效應，本研究將地震前與地震後兩時期的走時資料，各別考量相對應地震對的地震位置、震央距差值以及相對應波線對的波線方位角差值，挑選出地震前後兩時期相似路徑的地震波線，並將走時資料依空間分佈分為三種：(1)不相等波線、(2)相等波線不包含測站修正以及(3)相等波線包含測站修正，進行一系列的測試，研究走時層析成像在時間-空間上的解析情形，檢驗不相等的地震波線空間分佈如何影響三維速度構造。並以 2013 年 10 月 31 日發生於臺灣東部芮氏規模 6.4 的瑞穗地震，檢驗使用震波走時層析成像法解析地殼速度變化的可行性。透過棋盤格測試、解析能力測試以及反演程度差異的確認，解析出速度變化在空間中的可信區域。

速度變化的結果顯示，P 波速度在震源區域有約 2% 正值速度變化出現在深度 10 公里處，往下可延伸至 15 公里包圍震源並伴隨著量值增加至約 5%。在深度 20 公里處，正值速度變化以北北東-南南西的趨勢集中在距離震源位置大約 10-30 公里的北北東區域，而此正值區域包圍斷層主要滑移區的周圍。此外，在深度 10 公里處有約 3-8% 負值速度變化出現在餘震集中之區域的東北邊。大多數餘震發生在正值與負值速度變化的邊界。S 波速度在深度 10 公里處，有負值速度變化(~5-10%)出現在震源位置的西側及東北側，而位於震源位置西側的負值速度變化向下延伸至 15 公里伴隨著量值下降至約 3%。此外，在震源深度的正值速度變化(5-10%)出現在距離震源大約 10-30 公里的北北東區域，與震源主要破裂區域符合，而此正值

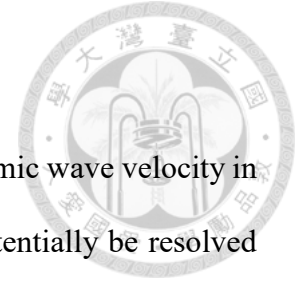


速度變化向下延伸、向北集中在離震源位置約 30 公里處。速度變化的結果顯示，在主震區域的地震 P 波和 S 波速度沿著斷層破裂方向變快、大多數餘震集中在速度變化梯度大的區域，而在斷層破裂終止、距離震源位置約 30 公里處，速度在約深度 12-15 公里以上的區域變慢、20 公里區域變快。我們認為這樣的的速度變化是由於地震前後震源區域及其周圍應力調整、裂隙密度改變以及斷層下盤地塊的彈性回跳所致。

值得注意的是不單只是地震波線在空間上的分佈會影響速度構造反演的結果，走時資料在挑波時的權重也會造成解析速度變化的偏差。然而，當我們考慮了兩時期的地震波線在空間上具有相同分佈位置，而各時期走時資料具有各自反演速度構造的能力，並且兩時期走時資料解析速度構造的能力相當，地震走時層析成像法即可用以解析三維空間速度構造隨時間的變化。

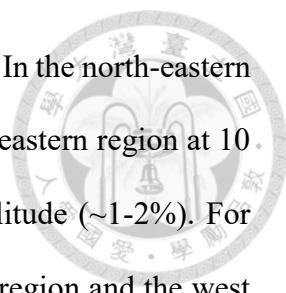
關鍵字：彈性回跳、地震波速度變化、時間相依震波層析成像、走時層析成像、瑞穗地震

Abstract



Using seismic travel time tomographic method, changes of seismic wave velocity in crust associated with moderate-to-large sized earthquakes could potentially be resolved with the tomographic images before and after the occurrence of an earthquake. However, unequal ray distribution during two time periods can also cause the artifacts in resulting of temporal seismic wave velocity changes. Thus, to selected the two travel time datasets with equal ray distribution, we considered the location distance of each event pair, the differences of epicentral distance and the gap of azimuths for each station-source pair. We then conducted a series of tests to investigate the temporal-spatial resolution of tomographic results, especially for examining how the unequal ray distributions can influence the three-dimensional V_P and V_S crustal structures. We demonstrated the feasibility of time-dependent tomographic method by applying it to image the velocity changes before and after an earthquake occurred on 2013 October 31, in Rueisuei in eastern Taiwan ($M_L = 6.4$), which was well recorded by the Central Weather Bureau Seismic Network (CWBSN) stations, Taiwan Strong Motion Instrumental Program (TSMIP) and Broadband Array in Taiwan for Seismology (BATS) stations. In our tomographic results, quite different patterns were found between the results of equal and unequal type of ray distributions. Through investigating the checkerboard resolution tests, resolution maps and discrepancy between the checkerboard-like models within two time periods, the reliable region were revealed.

In our results, in the source region of the 2013 Rueisuei earthquake, a positive velocity changes (the model difference, ΔM) in V_P (~ 2 -10%) appeared surrounding the source location at 15 km depth. This anomaly of velocity changes downwardly extended to ~ 10 -30 km away in the northern region of source at 20 km depth with a tendency in



the NNE-SSW direction, which rupture of the fault plane propagated. In the north-eastern region of aftershocks, a negative ΔM (~3-8%) appeared in the north-eastern region at 10 km depth and downwardly stretched to 15 km with decreased amplitude (~1-2%). For ΔM in V_s , two negative ΔM (~5-10%) appeared in the north-eastern region and the west side of the source location, and these anomalies downwardly extended to 15 km depth with decreasing in intensity. In the region where most aftershocks located, a strong positive anomaly (~5-10%) was shown with the same trending in the NNE-SSW direction just located at the major slip area. This anomaly downwardly stretched and further localized in the north where there was ~30 km away from the source location at 20 km depth. We suggested that the observed ΔM in the source region were mainly caused by increasing in stress due to the rupture of the mainshock and elastic rebounded of crust.

It is worth noting that not only will the distribution of rays affect the results of time-dependent travel time tomographic inversion but also different weighting value of the arrival-pickings from travel time data in the pre-seismic and the post-seismic periods bias the structures in tomographic inversion procedure. When the comparable resolution before and after a moderated-to-large sized earthquake can be achieved with identical ray distribution, the travel time tomographic method is then able to resolve the seismic wave velocity changes.

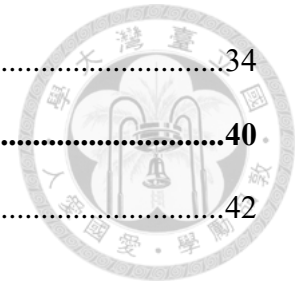
Keywords: elastic rebound, temporal change of seismic velocity, time-dependent tomography, travel time tomography, Rueisuei earthquake

Table of Contents



論文口試委員會審定書	i
誌謝	ii
中文摘要	iii
Abstract.....	v
Table of Contents.....	vii
List of Figures.....	ix
List of Tables	xiii
Chapter 1 Introduction.....	1
Chapter 2 Data and analysis procedure.....	5
2.1 The 2013 Rueisuei earthquake.....	5
2.2 Data.....	5
2.3 Selection of ray distribution.....	6
2.4 Flowchart analysis	11
Chapter 3 Method	14
3.1 Determination of earthquake location	15
3.2 Travel time tomographic inversion.....	16
3.3 Parameter setting	17
3.4 Model difference.....	18
Chapter 4 Resolution verification.....	21
4.1 Checkerboard resolution tests.....	21
4.2 Discrepancy of checkerboard-like structures.....	22
4.3 Summary.....	26
Chapter 5 Results and discussion	31
5.1 Model difference in V_P and V_S	31

5.2	Discussion.....	34
Chapter 6	Conclusions.....	40
References		42
Appendices	49	
A.	Initial 3-D velocity models for tomographic inversion.....	49
B.	Testing for different value of smoothing and damping factors	53
C.	Time-expending tomographic inversion	56
D.	Tomographic inversion with an initial 1-D velocity model and equal-type travel time data	63
E.	Synthetic test considering an initial 3-D velocity model and equal-type travel time data	65
F.	Testing the influence of weighting value of arrival-pickings in travel time data on tomography with the checkerboard-like structure considering an initial 3-D velocity model and equal-type travel time data.....	68



List of Figures



Figure 2.1 Distribution map of seismicity, seismic stations and ray coverages	8
Figure 2.2 Schematic illustration of the selected criteria of equal rays.....	9
Figure 2.3 Statistical plots of equal-type travel time data which without considering the station corrections.	10
Figure 2.4 Station corrections of relocating travel time residuals from catalogue.....	11
Figure 2.5 Flowchart of stepwise analysis.	13
Figure 3.1 The Root Mean Square (RMS) of total travel time residuals in each iteration.	19
Figure 3.2 The initial 1-D velocity model and value of V_P/V_S ratio.	19
Figure 3.3 Trade-off curve testing of the damping and smoothing factors.	20
Figure 4.1 Recovered checkerboard-like models using unequal-type travel time data (10210-/10254-arrivals)	23
Figure 4.2 Recovered checkerboard-like models using equal-type travel time data (4000- arrivals) without travel time correction.....	24
Figure 4.3 Recovered checkerboard-like models using equal-type travel time data (4000- arrivals) with travel time correction.....	25
Figure 4.4 Discrepancy in resulting of checkerboard tests (dV) and resolution maps (R) in V_P	27
Figure 4.5 Discrepancy in resulting of checkerboard tests (dV) and resolution maps (R) in V_S	28
Figure 4.6 Checkerboard model discrepancy in V_P and V_S of vertical profile using equal- type travel time data without station corrections.....	29
Figure 4.7 Checkerboard model discrepancy in V_P and V_S of vertical profiles using equal-	

type travel time data with station corrections.	30
Figure 5.1 The model difference (ΔM) in V_P	32
Figure 5.2 The model difference (ΔM) in V_S	33
Figure 5.3 The model differences in V_P , V_S and V_P/V_S of vertical profiles using equal-type travel time data without travel time correction.	37
Figure 5.4 The model differences in V_P , V_S and V_P/V_S of vertical profiles using equal-type travel time data with travel time correction.	38
Figure 5.5 A perspective view of the fault plane of the 2013 Rueisuei earthquake in the northern Longitudinal Valley with the velocity changes (P -wave at 20 km depth) and the aftershocks distribution (circles).....	39
Figure A 1. The initial 3-D model of unequal-type travel time data.	50
Figure A 2. Recovered checkerboard-like structure for the initial 3-D model of unequal-type travel time data.....	50
Figure A 3. The initial 3-D model of equal-type travel time data without station corrections.....	51
Figure A 4. Recovered checkerboard-like structure for the initial 3-D model of equal-type travel time data without station corrections.....	51
Figure A 5. The initial 3-D model of equal-type travel time data with station corrections.....	52
Figure A 6. Recovered checkerboard-like structure for the initial 3-D model of equal-type travel time data with station corrections.	52
Figure B 1. The results of ΔM using the initial 3-D model, equal-type travel time data without station corrections. The value of smoothing and damping factors were chosen to be 10 and 30 (Figure 3.3 (b)), respectively.....	54
Figure B 2. The results of ΔM using the initial 3-D model, equal-type travel time data	

without station corrections. The value of smoothing and damping factors were chosen to be 50 and 30 (Figure 3.3 (b)), respectively.....54

Figure B 3. The results of ΔM using the initial 3-D model, equal-type travel time data without station corrections. The value of smoothing and damping factors were chosen to be 20 and 15 (Figure 3.3 (b)), respectively.....55

Figure B 4. The results of ΔM using the initial 3-D model, equal-type travel time data without station corrections. The value of smoothing and damping factors were chosen to be 20 and 50 (Figure 3.3 (b)), respectively.....55

Figure C 1. Discrepancy of checkerboard-like structures, resolution maps and ΔM in V_P at 10 km depth considering the equal-type travel time data, an initial 3-D velocity model and no station corrections between two time periods.57

Figure C 2. Discrepancy of checkerboard-like structures, resolution maps and ΔM in V_P at 15 km depth considering the equal-type travel time data, an initial 3-D velocity model and no station corrections between two time periods.58

Figure C 3. Discrepancy of checkerboard-like structures, resolution maps and ΔM in V_P at 20 km depth considering the equal-type travel time data, an initial 3-D velocity model and no station corrections between two time periods.59

Figure C 4. Discrepancy of checkerboard-like structures, resolution maps and ΔM in V_S at 10 km depth considering the equal-type travel time data, an initial 3-D velocity model and no station corrections between two time periods.60

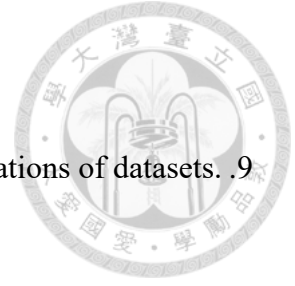
Figure C 5. Discrepancy of checkerboard-like structures, resolution maps and ΔM in V_S at 15 km depth considering the equal-type travel time data, an initial 3-D velocity model and no station corrections between two time periods.61

Figure C 6. Discrepancy of checkerboard-like structures, resolution maps and ΔM in V_S at 20 km depth considering the equal-type travel time data, an initial 3-D

velocity model and no station corrections between two time periods.	62
Figure D 1. The trade-off curve test considering the equal-type travel time data and an initial 1-D model.	64
Figure D 2. The results of ΔM considering an initial 1-D model, equal-type travel time data and no station corrections.	64
Figure E 1. The results of synthetic test in V_P considering an initial 3-D model, three anomalies and equal-type travel time data with station corrections in 10, 15 and 20 km depth.	66
Figure E 2. The results of synthetic test in V_S considering an initial 3-D model, three anomalies and equal-type travel time data with station corrections in 10, 15 and 20 km depth.	67
Figure F 1. Discrepancy of checkerboard-like structures, resolution maps in V_P at 10, 15 and 20 km depth considering an initial 3-D velocity model and the equal-type travel time data with station corrections and the same weighting value between two time periods.	69
Figure F 2. Discrepancy of checkerboard-like structures, resolution maps in V_S at 10, 15 and 20 km depth considering an initial 3-D velocity model and the equal-type travel time data with station corrections and the same weighting value between two time periods.	69

List of Tables

Table 2.1 Numbers of phases-arrivals, selected seismic events and stations of datasets. .9
--

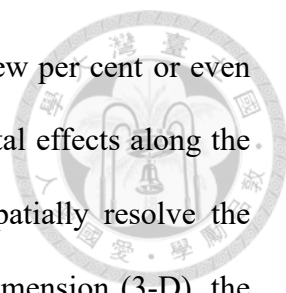


Chapter 1 Introduction



Temporal changes of seismic wave velocity in crust can be found after the occurrences of earthquakes and volcanic activities (Boore et al., 1975; Kanamori and Fuis, 1976; Poupinet et al., 1984; Lees and Nicholson, 1993; Zhao and Kanamori, 1995, 1996; Nishimura et al., 2000; Chen et al., 2001; Schaff and Beroza, 2004; Peng and Ben-Zion, 2006; Brenguier et al., 2008; Xu et al., 2009; Chen et al., 2011; Yu and Hung, 2012; Koulakov et al., 2013, Yu et al., 2013; Kasatkina et al., 2014; Taira et al., 2015; Koulakov et al., 2016; Wu et al., 2016). These variabilities in seismic wave velocity were caused by different geophysical processes, including stress changes, deformation and fluid transport during the pre-eruption and eruption stage of volcanoes (Patanè et al., 2006; Koulakov et al., 2013, Kasatkina et al., 2014), strong ground shaking due to earthquakes (Peng and Ben-Zion, 2006; Brenguier et al., 2008; Yu and Hung, 2012; Taira et al., 2015), dynamic or static stress changes related to earthquakes (Xu et al., 2009; Taira et al., 2015), damages in the fault zones (Xu et al., 2009; Chen et al., 2011; Yu and Hung, 2012), increasing in crack density and fluid migrations in vicinity of source region before and after earthquakes (Chen et al., 2001).

Over the past few decades, there are two methods have been wildly used to detect variations in seismic velocity. One is measuring time lapse of characteristic arrivals between stations, which can be represented by variations in seismic velocity, by using the empirical Green's function (EGF) retrieved from cross-correlation functions (CCFs) of continuous seismic coda waves, ambient noise or by changes in waveforms of repeating earthquakes (Poupinet et al., 1984; Schaff and Beroza, 2004; Peng and Ben-Zion, 2006; Brenguier et al., 2008; Chao and Peng, 2009; Chen et al., 2011; Yu and Hung, 2012; Yu et al., 2013; Soidati et al., 2015; Taira et al., 2015; Wu et al., 2016). The abilities of CCFs



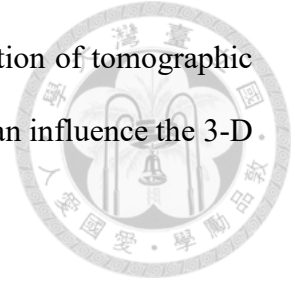
method can detect the values of velocity variation on the order of few per cent or even less. However, waveform cross-correlation-based method reveals total effects along the ray path between station pairs without spatial resolvability. To spatially resolve the seismic velocity changes before and after an earthquake in three-dimension (3-D), the time-dependent seismic tomography is a more potentially alternative. Using time-dependent seismic tomography, Foulger et al. (1997) and Gunasekera et al. (2003) examined the V_P and V_P/V_S structures of the Geysers geothermal area in California from 1991 to 1998 and found that the variations of V_P/V_S ratio indicated the changes of pressures and/or liquid saturation in reservoir. Patanè et al. (2006) monitored magma intrusions and eruption cycle of Mount Etna from August 2001 to January 2003 including several explosive activities and found that anomalies with low V_P/V_S value beneath the central part of volcanic mount was increasing during the 2002-2003 eruption. Koulakov et al. (2013) presented time-dependent tomography for the Kluchevskoy and Bezymianny volcanoes in Kamchatka, Russia, from 1999 to 2009 and successfully found the characteristics of magmatic activities and revealed channels of volcanic system beneath the Kluchevskoy volcano. Koulakov et al. (2016) conducted time-dependent tomography in Tohoku region, in Japan, before and after the 2011 Tohoku-Oki earthquake. They suggested that the observed velocity changes might correspond to compression of crustal rocks, the large aftershocks and volatile release from the coupling zone of the slab. Consequently, time-dependent seismic tomography provides a practical approach for us to evaluate the changes of seismic wave velocity in Earth structure.

The travel time tomographic method has been well developed and applied to not only image regional and uppermost mantle structures in Taiwan (Chen et al., 1994; Rau and Wu, 1995; Ma et al., 1996; Cheng, 2000; Chen et al., 2001; Kim et al., 2005; Wu et al., 2007, 2009; Kuo-Chen et al., 2012; Huang et al., 2014; Koulakov et al., 2014) but

also understand the rock mechanical properties (Lees and Nicholson, 1993; Zhao and Kanamori, 1995, 1996; Chen et al., 2011). These previous studies have suggested that variability in the material properties of the fault zone might be responsible for variations in the seismogenic behaviors (Lees and Nicholson, 1993; Zhao and Kanamori, 1995, 1996; Chen et al., 2011). In Taiwan, Chen et al. (2001) observed the temporal velocity changes around source area of the 1999 M_L 7.3 Chi-Chi earthquake. They proposed that the changes in V_P and V_P/V_S anomalies corresponded to the localized stress changes caused by the major slip of rupture and also found that larger aftershocks mostly occurred in the regions of high gradient of V_P and V_P/V_S anomalies. The inception of dense seismic networks in Taiwan in the early 1990s supplies a good opportunity to investigate temporal velocity changes associated with moderate-sized crustal earthquakes ($M_L > 6$ and focal depth ≤ 40 km) in Taiwan.

However, it is still being debated that whether real changes of material properties in the Earth could be correctly revealed through tomographic method due to the distinct earthquake locations and seismic networks, and observational errors in each time period. Unequal ray distributions during two time periods can be one of the main factors causing the artifacts of temporal seismic velocity changes (Julian and Foulger, 2010; Koulakov et al., 2016). Thus, in this study, we considered the location distance of each event pairs, the differences of epicentral distance and the gap of azimuth for each station-source pairs to select travel time data with equal ray distribution. We applied travel time tomographic algorithm developed by Huang et al. (2014) to obtain 3-D V_P and V_S crustal structures of time periods before and after the 2013 M_L 6.4 Rueisuei earthquake, with a focal depth of 14.98 km in eastern Taiwan, which was well recorded by the Central Weather Bureau Seismic Network (CWBSN) stations, Taiwan Strong Motion Instrumental Program (TSMIP) and Broadband Array in Taiwan for Seismology (BATS) stations. We also

conducted a series of tests to investigate the temporal-spatial resolution of tomographic results, especially for examining how the unequal ray distributions can influence the 3-D V_P and V_S crustal structures.



Chapter 2 Data and analysis procedure

2.1 The 2013 Rueisuei earthquake

The Rueisuei earthquake occurred on 31 October 2013 in the Longitudinal Valley (LV) in eastern Taiwan where was considering to be the suture zone of the Philippine Sea Plate and the Eurasian Plate. The mainshock was reported by the CWB with epicentral location at 121.348°E, 23.566°N, focal depth of 14.98 km and local magnitude (M_L) equal to 6.4. The fault plane, with a strike of 209° and a westward dip of 59°, was determined from the CWB Centroid Moment Tensor (CMT) solution (Figure 2.1(a)). Hundreds of aftershocks occurred in the following few days and most of the aftershocks were located in the northern region of the mainshock with a trending in NNE-SSW direction fitting well with the strike of the LV.

2.2 Data

For tomographic inversion, the selection of the background earthquakes before and after the 2013 Rueisuei earthquake ($M_L = 6.4$) from relocated catalog of Wu et al. (2008, recently updated to 2015) was based on the following criteria: (1) earthquakes occurred in a grid with a $\pm 0.6^\circ$ range for both latitude and longitude, with considering epicenter of mainshock as the center and 0-60 km range in the depth; (2) local magnitude of events is larger than or equal to 2.0; (3) all events have a station coverage gap of less than 270°; (4) each event was recorded by at least 8 stations with both good-quality reading of P -wave and S -wave. Figure 2.1(a) shows the background seismicity from 1994 to the end of 2013 after selection.

The relocated earthquake catalog (Wu et al., 2008, recently updated to 2015) was combining a large dataset of P -wave, S -wave phases arrivals and S - P times from several



seismic networks. In this study, we used the *P*-wave and *S*-wave travel time data recorded by the CWBSN, TSMIP and BATS stations. The CWBSN is a permanent seismic network in charge of routinely monitoring seismicity in Taiwan (Shin, 1992, 1993). The TSMIP consists of over 800 free-field stations densely spread over the Taiwan region with an average inter-station spacing of about 5 km except for the high mountain regions (Shin, 2003). The BATS stations are the Broadband Array in Taiwan for Seismology operated by the Institute of Earth Sciences (IES) of Academia Sinica and frequently used in seismological research (Kao et al., 1998).

2.3 Selection of ray distribution

In order to examine the influence of ray distribution on tomographic results, we performed three types of datasets based on the critical value of location distance of each event pair, the differences of epicentral distance and the gap of azimuth for each station-source pair chosen to be 0.03° and 4 km and 2° : (1) unequal-type travel time data (10210-/10254-*arrivals*, including 5105-/5127-*arrivals* for both *P*-wave and *S*-wave in two time periods, respectively), (2) equal-type travel time data (4000-*arrivals*, including 2000-/2000-*arrivals* for both *P*-wave and *S*-wave) without station corrections of time residuals and (3) equal-type travel time data (4000-*arrivals*, including 2000-/2000-*arrivals* for both *P*-wave and *S*-wave) with station corrections of time residuals to remove the site effect of each station. Schematic illustration of the selected criteria of equal rays was shown in Figure 2.2. Figure 2.3 demonstrates the difference of event location, epicenter distance, gap of azimuths and time difference of *P*-wave and *S*-wave arrivals for each pair of seismic rays which represented by the equal-type travel time data but without station corrections. Value of correcting time residuals were from the station correction term of

joint hypocenter relocation method (Frohlich, 1979; Wu et al., 2003) for a recently relocated earthquake catalog (Wu et al., 2008, recently updated to 2015) which represented the localized shallow structure beneath each station (Figure 2.4). The time periods before and after the 2013 Rueisuei earthquake were determined by considering a uniform counts of seismic rays in the study area (8 June 2013 to 30 October 2013 and 31 October 2013 to 31 January 2014 for pre-seismic and post-seismic time periods of unequal-type travel time data, respectively; 31 January 2013 to 30 October 2013 and 31 October 2013 to 31 January 2014 for pre-seismic and post-seismic time periods of equal-type travel time data, respectively). In order to obtain more uniform distribution of seismicity for inverting the dataset with unequal ray distribution, a source selection method proposed by Liang et al. (2004) was adopted with 1 km radius. Table 2.1 summarizes numbers of selected events, seismic stations, and phase arrivals of equal and unequal type of datasets for tomographic inversions. Distributions of selected earthquakes, seismic stations and ray coverages before and after the occurrence of the 2013 Rueisuei earthquake were shown in Figure 2.1(b-e).

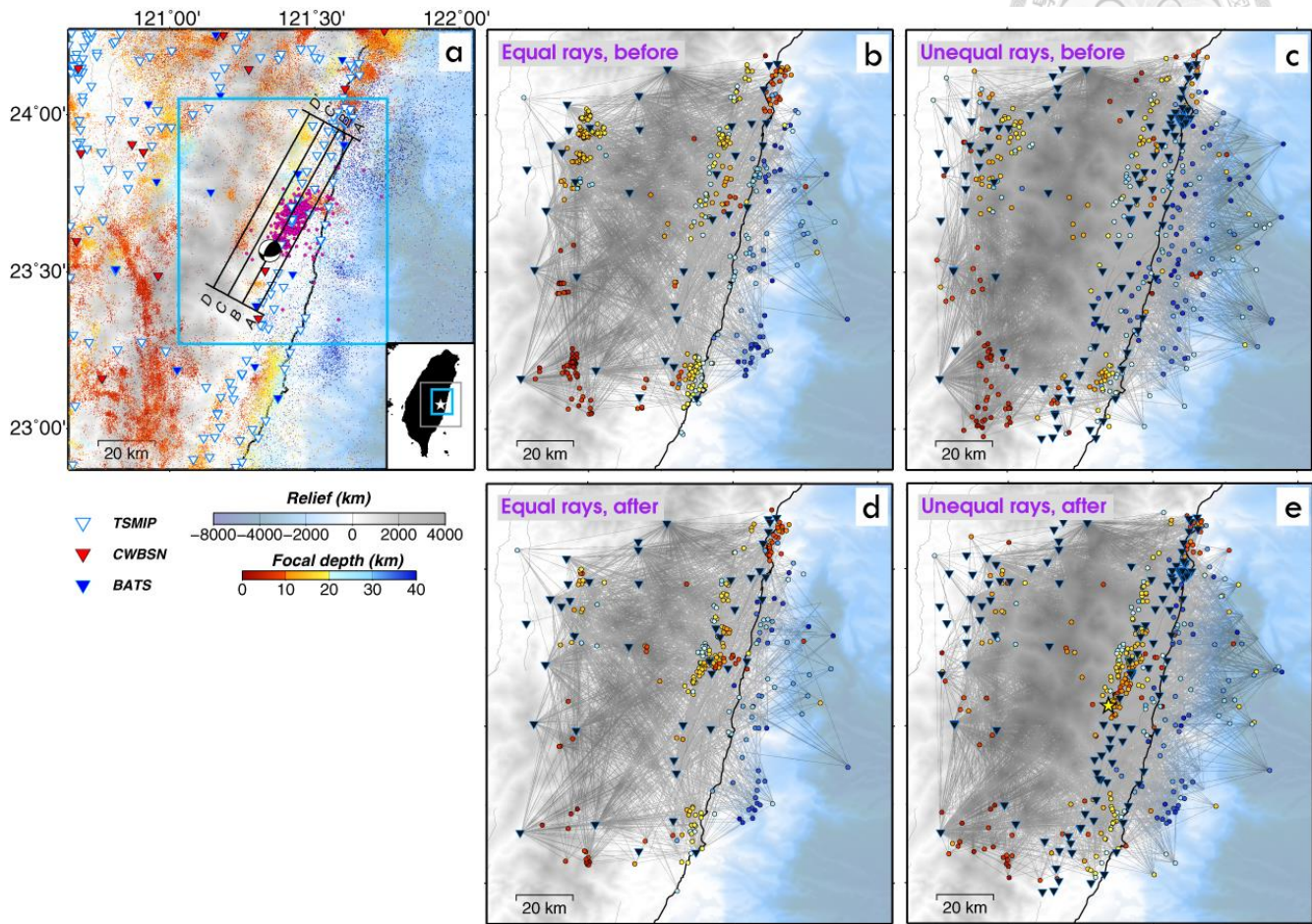


Figure 2.1 Distribution map of seismicity, seismic stations and ray coverages in different time periods before and after the 2013 Rueisuei earthquake. Seismic events used in travel time tomographic inversions are denoted by circles with focal-depth-based color in (b-e). Background color shows the relief, and grey lines indicate the fault traces on surface. (a) Color dots display the seismicity from 1994 to the end of 2013 in the study region. Inverted triangles with red, white and blue colors represent stations of the Central Weather Bureau Seismic Network (CWBSN), Taiwan Strong Motion Instrumental Program (TSMIP) and Broadband Array in Taiwan for Seismology (BATS), respectively. The beach ball shows the focal mechanism of the 2013 Rueisuei mainshock reported by the CWB, with a strike of 209° and a westward dip of 59° . The light blue block represents the boundary of Figures 4.4, 4.5, 5.1, 5.2 and 5.5. Circles with purple color show the earthquakes occurred in 10 days following the mainshock in the blocked region. (b-e) show the ray coverages with equal and unequal ray distributions before and after the 2013 Rueisuei mainshock. (b) and (d) Ray coverage with 4000-arrivals which represent the equal ray distribution. (c) and (e) Ray coverage with 10210-/10254-arrivals which represent the unequal ray distribution.

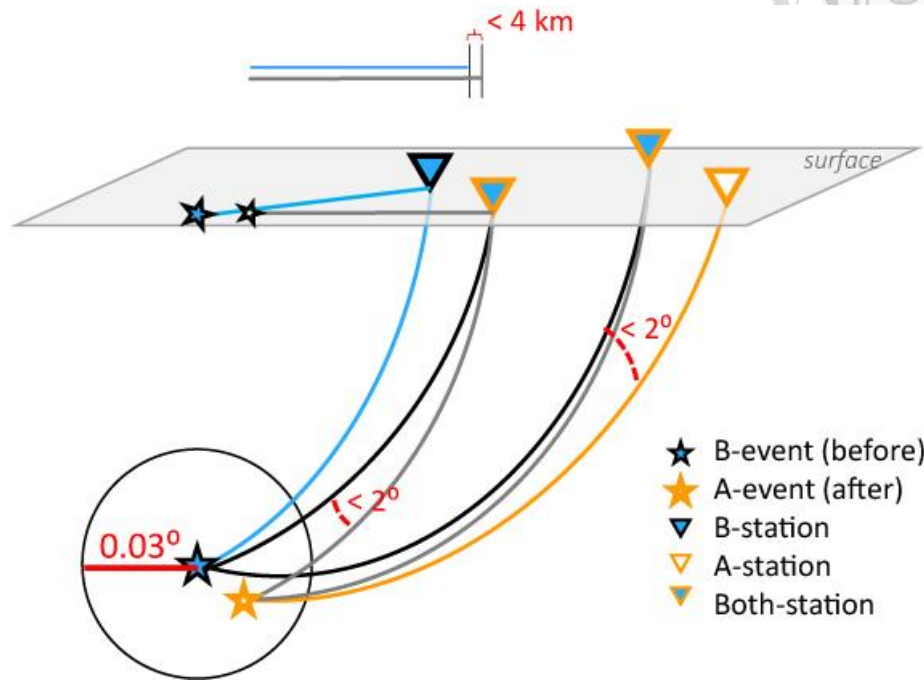


Figure 2.2 Schematic illustration of the selected criteria of equal rays. Blue stars and inverted triangles with black solid line indicate the event and stations in the pre-seismic time period. White stars and inverted triangles with orange solid line indicate the event and stations in the post-seismic time period. Blue inverted triangles with orange solid line represent the stations exist both in pre-seismic and post-seismic time periods. Blue and grey strait lines indicate the epicenter distance of earthquake occurred in the pre-seismic and post-seismic time periods, respectively.

Table 2.1 Numbers of phases arrivals, selected seismic events and stations of datasets.

TYPE OF RAY DISTRIBUTION	<i>Equal</i>	<i>Unequal</i>
<i>Pre-seismic time period</i>	2013/1/31-2013/10/30	2013/6/8-2013/10/30
<i>Phases arrivals</i>	4000	10210
<i>Earthquake events</i>	489	405
<i>Seismic stations</i>	37	38
<i>Post-seismic time period</i>	2013/10/31-2014/1/31	2013/10/31-2014/1/31
<i>Phases arrivals</i>	4000	10254
<i>Earthquake events</i>	468	371
<i>Seismic stations</i>	42	64



Figure 2.3 Statistical plots of equal-type travel time data which without considering the station corrections. (a) The difference of event location, epicenter distance, and gap of azimuths for each pair of seismic rays, respectively. (b) The time difference of *P*-wave and *S*-wave arrivals versus the difference of event location, and counts of time difference in arrivals, respectively.

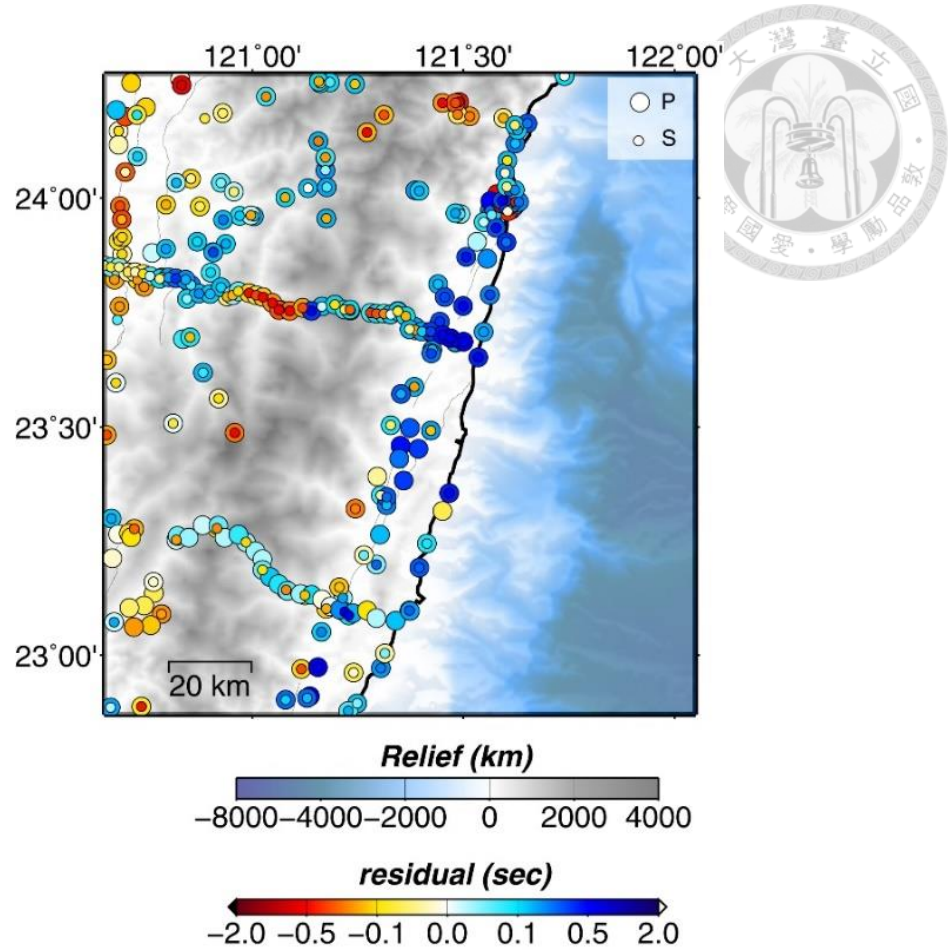


Figure 2.4 Station corrections of relocating travel time residuals from catalogue. Large and small circles display the value of station corrections in *P*-wave and *S*-wave with colors, respectively. The color in the background represents the topography.

2.4 Flowchart analysis

The aim of this study is to evaluate the influence of different ray distribution on the results of time-dependent tomography. As mentioned in section 2.3, based on the location distance of each event pair, the differences of epicentral distance, and the gap of azimuth for each station-source pair, the input travel time data were selected in three types: unequal-type, equal-type without station corrections, and equal-type with station corrections in two time periods before and after the 2013 mainshock. Then, travel time tomographic inversion was repeated to obtain the 3-D velocity structures in pre-seismic

and post-seismic time periods and retrieve the changes of seismic velocities in between. In this study, considering the reduction of total residual Root Mean Square (RMS) in iterations and constraints of the source-station paths, 15 iterations were conducted for each dataset without updated event locations.

The stepwise procedures (Figure 2.5) were presented as follows: (1) relocating all selected earthquakes by the relocation program 3DCOR (Wu et al., 2003) with the 3-D velocity model proposed by Wu et al. (2009); (2) adopting a source selection method proposed by Liang et al. (2004) to have a uniform event distribution in space for unequal type of ray distribution and considering the critical value of location distance of each event pair, the differences of epicentral distance and the gap of azimuths for each station-source pair chosen to sort out the equal type of ray distribution; (3) setting a 1-D velocity model to be the initial velocity value in the first iteration for tomographic inversion with whole time periods data including pre-seismic and post-seismic time periods to construct the referred 3-D model; (4) inverting the 3-D velocity structure with 15 iterations and without updated event locations; (5) retrieving difference between two models before and after the mainshock. Therefore, the changes in seismic velocity were determined; (6) correcting the travel time residuals to remove the site effect of each station; then go through step (3), (4) and (5) to get model difference between two time periods.

However, except for tomographic inversions with real data of each time period, we also performed the checkerboard resolution tests and synthetic tests to verify our results in each time period in the step (4) with 15 iterations.

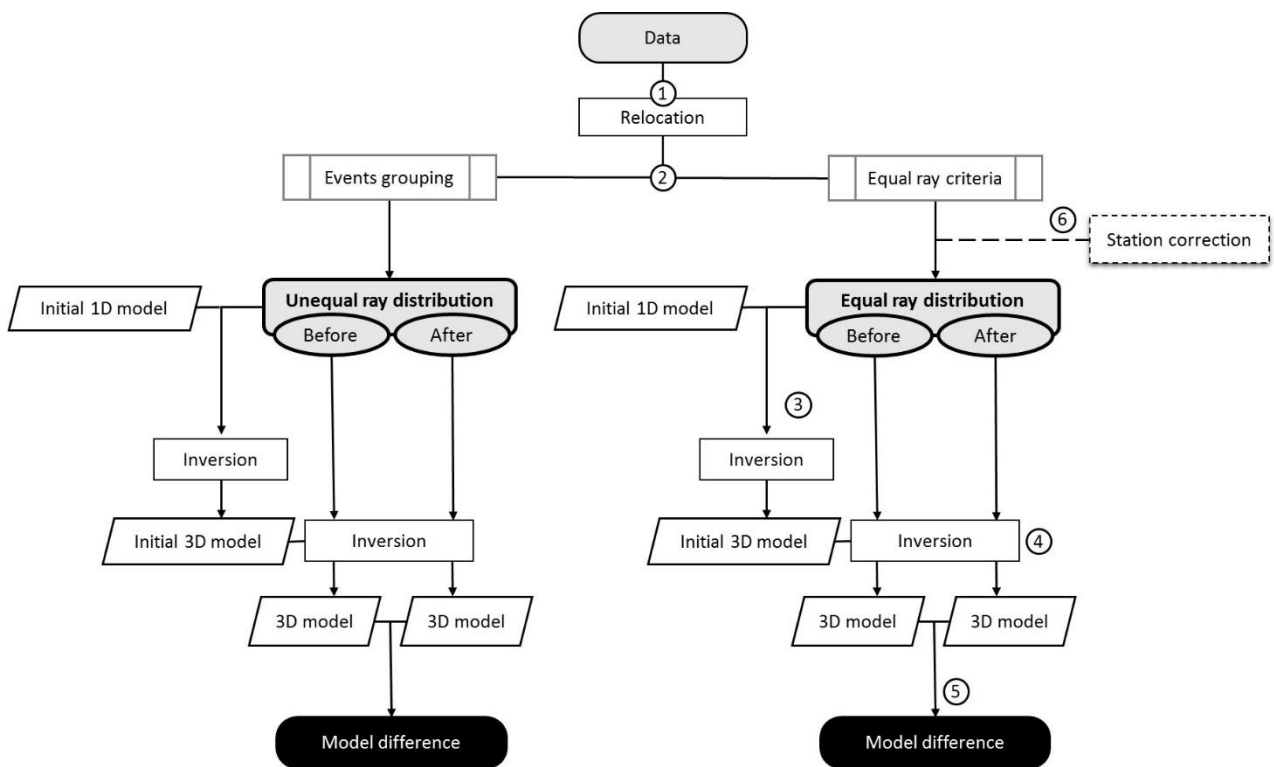


Figure 2.5 Flowchart of stepwise analysis.

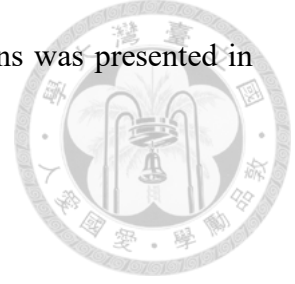
Chapter 3 Method

The regional travel time tomographic algorithm of Huang et al. (2014) was adopted in this study to image crustal structures of time periods before and after the 2013 Rueisuei earthquake. In order to improve fine initial earthquake locations for tomographic algorithm we applied the three-dimensional earthquake relocation program with station corrections, 3DCOR, proposed by Wu et al. (2003), to relocate initial seismic data by using the 3-D velocity model (Wu et al., 2009). The theoretical arrival time of *P*-wave and *S*-wave were calculated through 3-D ray tracing (Um and Thurber, 1987; Koketsu and Sekine, 1998) and the station corrections were determined from the averaged time residuals at each station.

After earthquake relocation, the initial 1-D model and whole time periods of data including pre-seismic and post-seismic time periods were used to derive a reference 3-D model for each dataset (shown in Appendix A). This 3-D model was used as an initial model to invert the 3-D structure for both pre-seismic and post-seismic time periods, respectively for each dataset. Travel time tomography was applied repeatedly for each dataset to obtain the 3-D structures of V_P and V_S of two time periods before and after the mainshock. Further, the model difference (ΔM) between different time periods that represented seismic velocity changes were retrieved. In addition, a number of tests, including checkerboard resolution tests and resolution maps, were conducted to verify the robustness of our results, which will be described in Chapter 4.

Other tests were also carried out for considering the same initial 3-D velocity model with different value of smoothing and damping factors (Appendix B), and the same initial 3-D velocity model with datasets which overlapped adding travel time data represented expanding on time (Appendix C). Finally, the result of tests considering the initial 1-D

velocity model and equal-type travel time without station corrections was presented in Appendix D.



3.1 Determination of earthquake location

The travel time of seismic phases is the spending time of seismic waves propagating from an hypocenter of earthquake n to the seismic station k with a known velocity model, $\mathbf{m} = (x, y, z, t)$. The arrival time T^n can be expressed as the summation of earthquake origin time τ^n and travel time of the seismic phases, as following equation:

$$T^n = \tau^n + \int_n^k u ds \quad (1)$$

where u and s are the slowness and the length on the path which seismic wave passes through. In general, this non-linear problem should be linearized by expanding in a Taylor series with neglecting the high-order terms. Then we can linearized the relationship between the adjustment of earthquake location, $\Delta \mathbf{m}^n = (\Delta x^n, \Delta y^n, \Delta z^n, \Delta \tau^n)$, the predicted travel time t_k^n , and the travel time residual r_k^n , as following equation, which presents the discrepancy in location and earthquake origin time:

$$\frac{\partial t_k^n}{\partial x} \Delta x^n + \frac{\partial t_k^n}{\partial y} \Delta y^n + \frac{\partial t_k^n}{\partial z} \Delta z^n + \Delta \tau^n = r_k^n \quad (2)$$

It can also be expressed as:

$$\frac{\partial t_k^n}{\partial \mathbf{m}} \Delta \mathbf{m}^n = r_k^n \quad (3)$$

The travel time residual r_k^n indicates the difference between the observed and the predicted data, $r_k^n = (t^{obs} - t^{pred})_k^n$. The predicted travel time t^{pred} were calculated based on ray tracing through a known velocity model. According to the adjustments of event location, the new location of earthquake can be obtained as following equation:

$$\mathbf{m}_{new} = \mathbf{m}_{old}^n + \Delta \mathbf{m}^n \quad (4)$$

Then, the event location would be updated for next iteration. After a number of iterations, the value of travel time residuals will converge to a stable value which means the location of earthquakes would not change too much in the following iterations and these locations represent the hypocenters of earthquakes. In this study, we obtained the eventual locations of our seismic data by 3 iterations.

3.2 Travel time tomographic inversion

As mentioned above, travel time residuals ΔT on ray i passing through the model m can be obtained by observed travel time t_i^{obs} subtract predicted one t_i^{pred} . And its information going through the grid j with the slowness Δu_j in model space can be expressed as the data kernel G_{ij} . The equation can be represented as follow:

$$\Delta T_i = t_i^{obs} - t_i^{pred} = \sum_j G_{ij} \Delta u_j \quad (5)$$

We can write the equation (5) in a form of $\mathbf{d} = \mathbf{Gm}$ where \mathbf{d} represents data vector, \mathbf{G} represents kernel matrix, and \mathbf{m} represents the model vector. The model vector can be separated into two terms of slowness S and source H , respectively. Here, the perturbations of the model vector in S and H terms are represented as Δs_i and Δh_i :

$$\mathbf{d} = t_i^{obs} - t_i^{pred} = \sum \left(\frac{\partial t}{\partial s} \right)_i \Delta s_i + \sum \left(\frac{\partial t}{\partial h} \right)_i \Delta h_i = \mathbf{G} \begin{bmatrix} S \\ H \end{bmatrix} \quad (6)$$

The linear system of tomographic inversion here can then be expressed as a matrix form as:

$$\begin{pmatrix} G_P & 0 & G_h \\ 0 & G_S & G_h \end{pmatrix} \begin{pmatrix} m_P \\ m_S \\ m_h \end{pmatrix} = \begin{pmatrix} d_P \\ d_S \end{pmatrix} \quad (7)$$

where G , m and d represent the partial derivatives of travel times, model perturbations and residual vectors for P -/ S -wave and source location.

The damping λ and smoothing φ factors are introduced for stabilizing inversion process of sparse matrix.

$$\begin{pmatrix} W\tilde{G} \\ \lambda I \\ \varphi L \end{pmatrix} \tilde{\mathbf{m}} = \begin{pmatrix} W\tilde{\mathbf{d}} \\ 0 \\ 0 \end{pmatrix} \quad (8)$$

I and L are the unit matrix and Laplacian operator. W is the data weighting. \tilde{G} , $\tilde{\mathbf{m}}$ and $\tilde{\mathbf{d}}$ represent the matrix form of the data kernel, model vector and data vector. The optimal λ and φ factors are chosen from the concave value of trade-off curve.

In the tomographic algorithm of Huang et al. (2014), the model is constructed in a spherical coordinate. The seismic rays are traced by a 3-D pseudo-bending ray-tracing algorithm (Um and Thurber, 1987; Koketsu and Sekine, 1998). Models of V_P and V_S are simultaneously inverted with updated event locations in every iteration. In this study, owing to the small reduction of total residual Root Mean Square (RMS) between the 12th to 15th iterations (Figure 3.1) and constraints of the source-station paths, 15 iterations were performed for each dataset without updated event locations.

3.3 Parameter setting

For the tomographic inversion procedure, we constructed a mesh with a horizontal spacing of 0.06° and vertical grid points were distributed at the depths of -0.5, 0, 3, 6, 10, 15, 20, 25, 30, 35, 40, 45, 50, 55 and 60 km. The initial 1-D P -wave model was directly averaged from the result of Huang et al. (2014). Then, an initial 1-D S -wave model was converted from P -wave model by assuming V_P/V_S value of 1.728 (Figure 3.2). Using this initial 1-D model and the data of entire time periods including pre-seismic and post-seismic time periods, we first derived a 3-D model as a reference model for each time period, and then this 3-D model was used as an initial model to invert the 3-D velocity

structures for pre-seismic and post-seismic time periods, respectively.

The optimal value of λ and φ factors were chosen to be 20 and 10 for unequal-type travel time data and 30 and 20 for equal-type travel time data for both V_P and V_S models from trade-off curve tests (data variance reduction versus model variance relationship; Figure 3.3).

3.4 Model difference

The 3-D structures of V_P and V_S of two time periods before and after the mainshock were retrieved from our tomographic inversions. The temporal changes of seismic velocities were presented as model difference (ΔM) defined as

$$\Delta M = \frac{(M^{after} - M^{before})}{M^{before}} \times 100\% \quad (9)$$

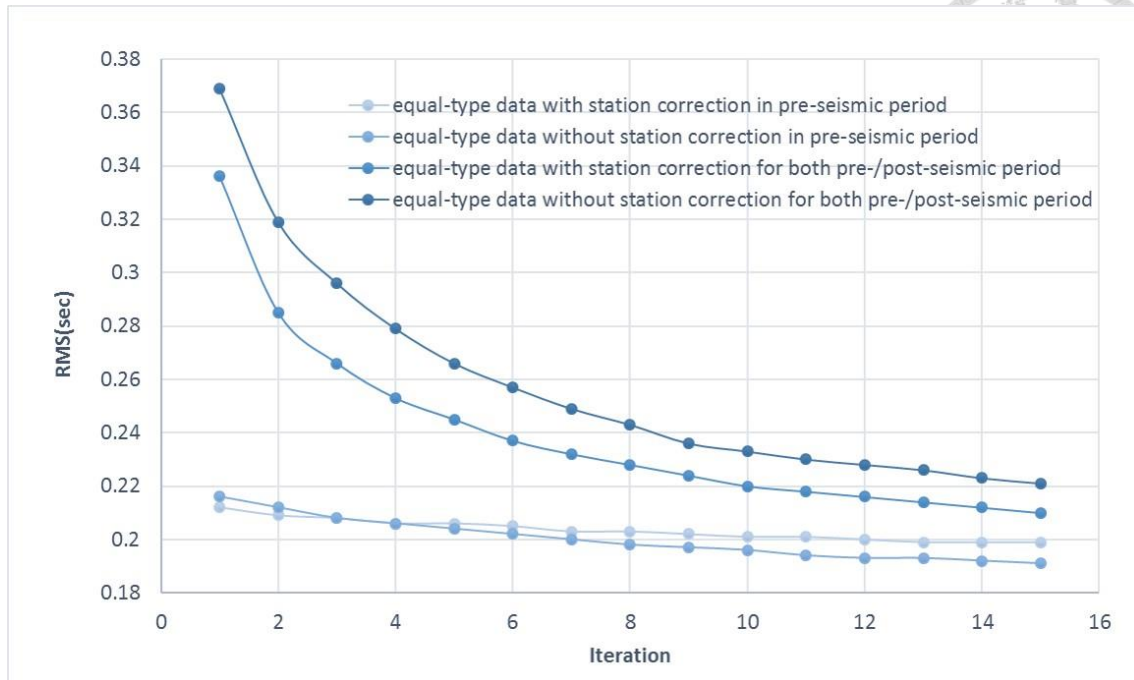


Figure 3.1 The Root Mean Square (RMS) of total travel time residuals in each iteration.

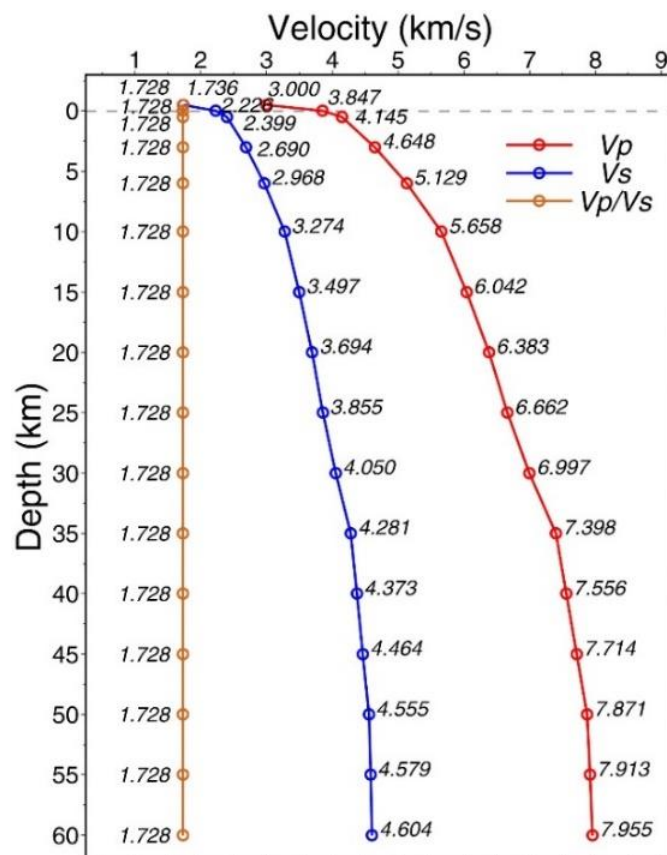
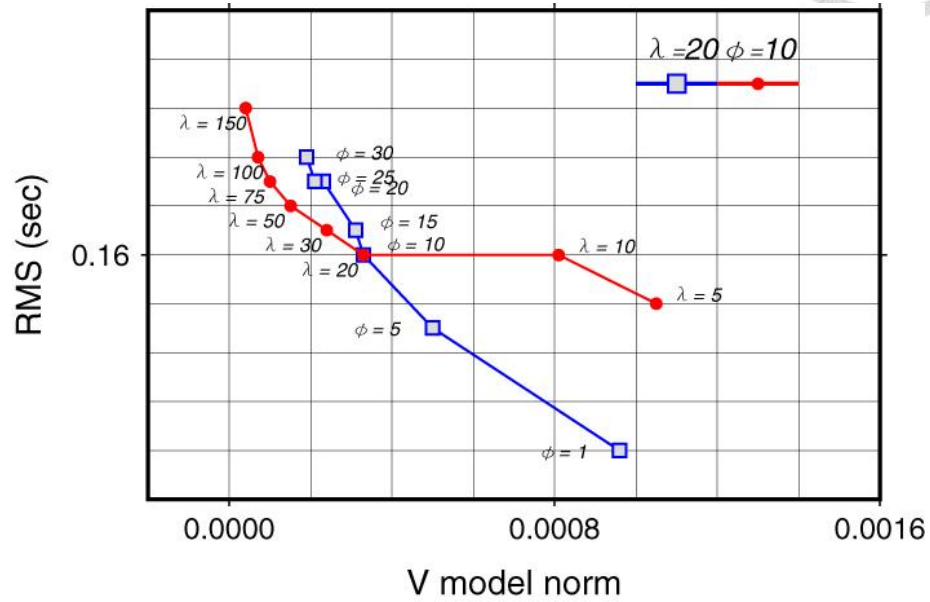


Figure 3.2 The initial 1-D velocity model and value of V_p/V_s ratio.



(a)



(b)

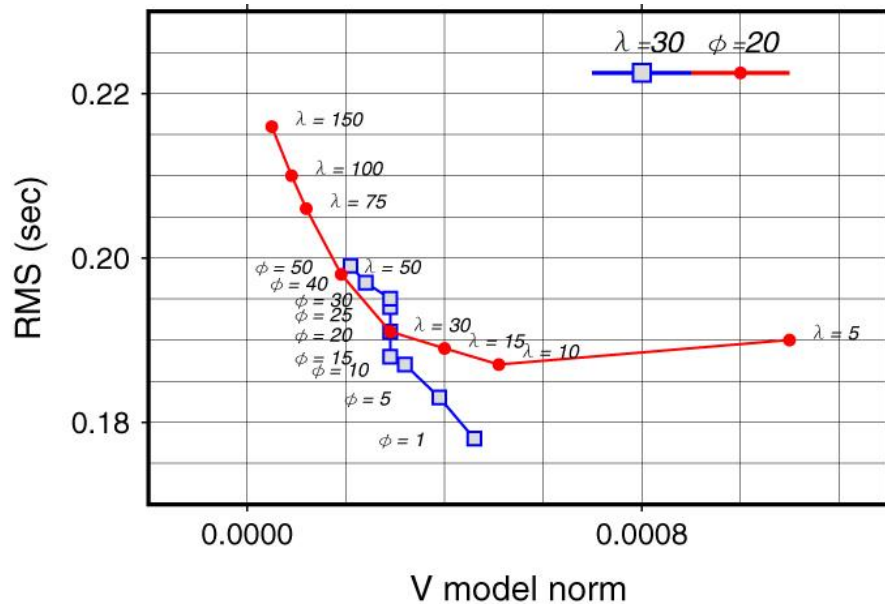
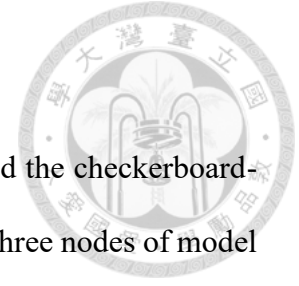


Figure 3.3 Trade-off curve testing of the damping (λ) and smoothing (ϕ) factors. (a) Unequal-type travel time data. (b) Equal-type travel time data without station corrections.

Chapter 4 Resolution verification



We performed the checkerboard resolution tests and constructed the checkerboard-like velocity models in V_P and V_S with $\pm 10\%$, a block size spanning three nodes of model in horizontal ($0.18^\circ \times 0.18^\circ$) and in vertical (varies with depth). The recovery level of synthetic models was translated into a resolvability factor, R (Zelt, 1998). According to the previous study in Taiwan (Huang et al., 2014), we chose a threshold value of R factor equal to 0.6 as a lower bound of well-resolved area. In the tomographic algorithm of Huang et al. (2014), models of V_P and V_S were simultaneously inverted. Owing to the small reduction between the 12th to 15th iterations, in this study, 15 iterations were performed for both checkerboard resolution tests and real data inversions without updated event locations.

To ensure the seismic velocity changes of each time dependent tomographic result were reliable, the same recovery level should be achieved in the results of both two time periods. Thus, we checked the results of checkerboard resolution tests, resolution maps and discrepancy of checkerboard resolution between two time periods (Figures 4.1-4.5).

Here, we also performed the synthetic test to verify the robustness of inverted structures (in Appendix E, only show the result of synthetic test considering the equal-type travel time data with station corrections).

4.1 Checkerboard resolution tests

Figures 4.1, 4.2 and 4.3 show the results of checkerboard resolution tests in V_P and V_S at depth of 10, 15 and 20 km for both two time periods of each dataset. As expected, the checkerboard-like patterns both in V_P and V_S were best well recovered in the results of unequal-type travel time data (10210-/10254-arrivals) as more travel time data were

used. Results of checkerboard-like models which inverted with equal-type travel time data show generally good recovery around the source especially in northern region at 15 km depth. Different recovered amplitudes in the results of checkerboard resolution tests for two time periods (Figures 4.4 and 4.5) imply different weighting value of the arrival-pickings from travel time data in the two time periods (shown in Appendix F).

4.2 Discrepancy of checkerboard-like structures

The different recovery levels in V_P and V_S structures between two time periods can clearly be seen in Figures 4.4 and 4.5, showing the R value in resolution maps and discrepancy of checkerboard-like models (velocity difference, dV) which defined as $dV = V_{CKB}^{after} - V_{CKB}^{before}$ between two time periods at 10, 15 and 20 km depth. Here, considering the effect of different recovery levels in two time periods, different weighting values on arrival-pickings from travel time data and the effect caused by our selection criterion of equal ray distribution, we shaded the region which have the dV value over of range $\pm 1.5\%$ and the R value less than 0.6. Therefore, in our results, only where the value of ΔM larger than 2% or smaller than -2% would be discussed.

The results of resolution maps presented that the resolvability became quite well when more input travel time data were used in inversion and the R value almost over 0.8 around the source region. Although the results of checkerboard resolution tests which inverted with more travel time data (10210-/10254-arrivals in unequal type of ray distribution) had better performance in recovering checkerboard-like structures (Figure 4.1), the discrepancy of recovering checkerboard-like structures showed different degree of recovery almost around the whole source region (Figures 4.4 and 4.5).

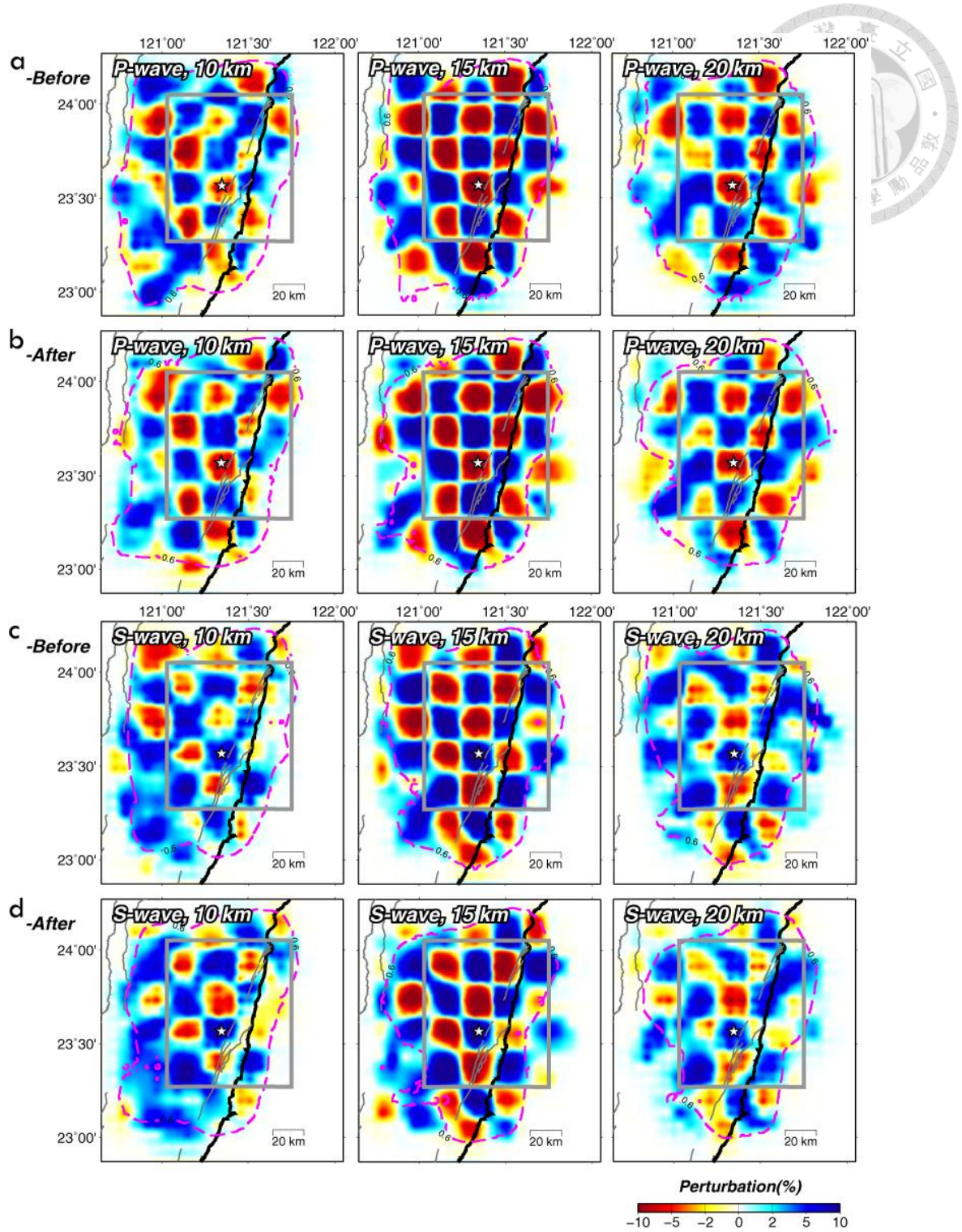


Figure 4.1 Recovered checkerboard-like models using unequal-type travel time data (10210-/10254-arrivals) at 10, 15 and 20 km depth in two time periods before and after the 2013 Rueisuei earthquake. White stars represent the epicenter of the 2013 Rueisuei mainshock. Red dash lines encircle the region with R value larger than 0.6. The grey boxes indicate the boundary of Figures 5.1 and 5.2. (a) and (c) show the results in V_P and V_S before the 2013 Rueisuei earthquake. (b) and (d) show the results in V_P and V_S after the 2013 Rueisuei earthquake.

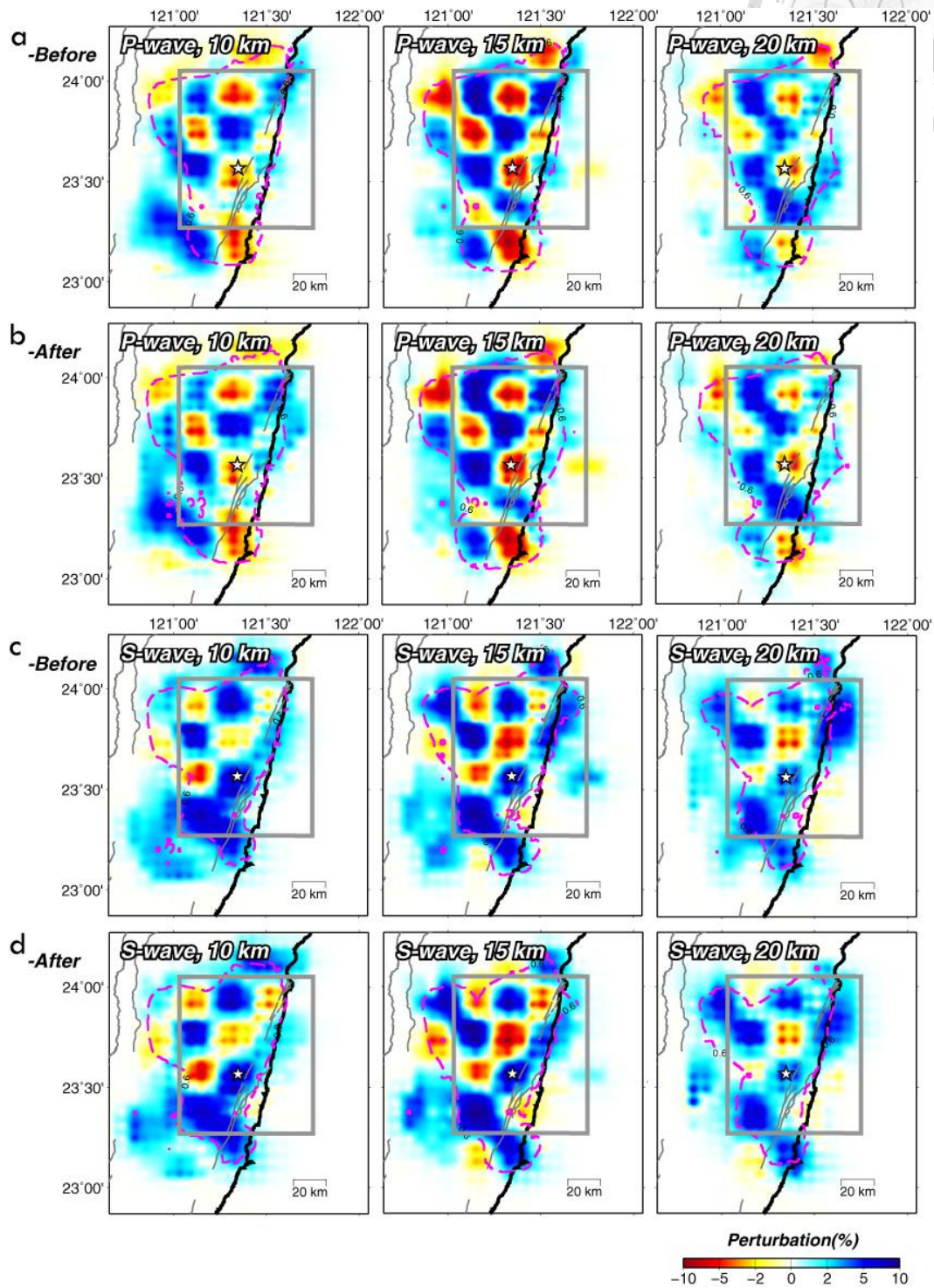


Figure 4.2 Recovered checkerboard-like models using equal-type travel time data (4000-arrivals) without travel time correction at 10, 15 and 20 km depth in two time periods before and after the 2013 Rueisuei earthquake. (a-d) see figure caption in Figure 4.1.

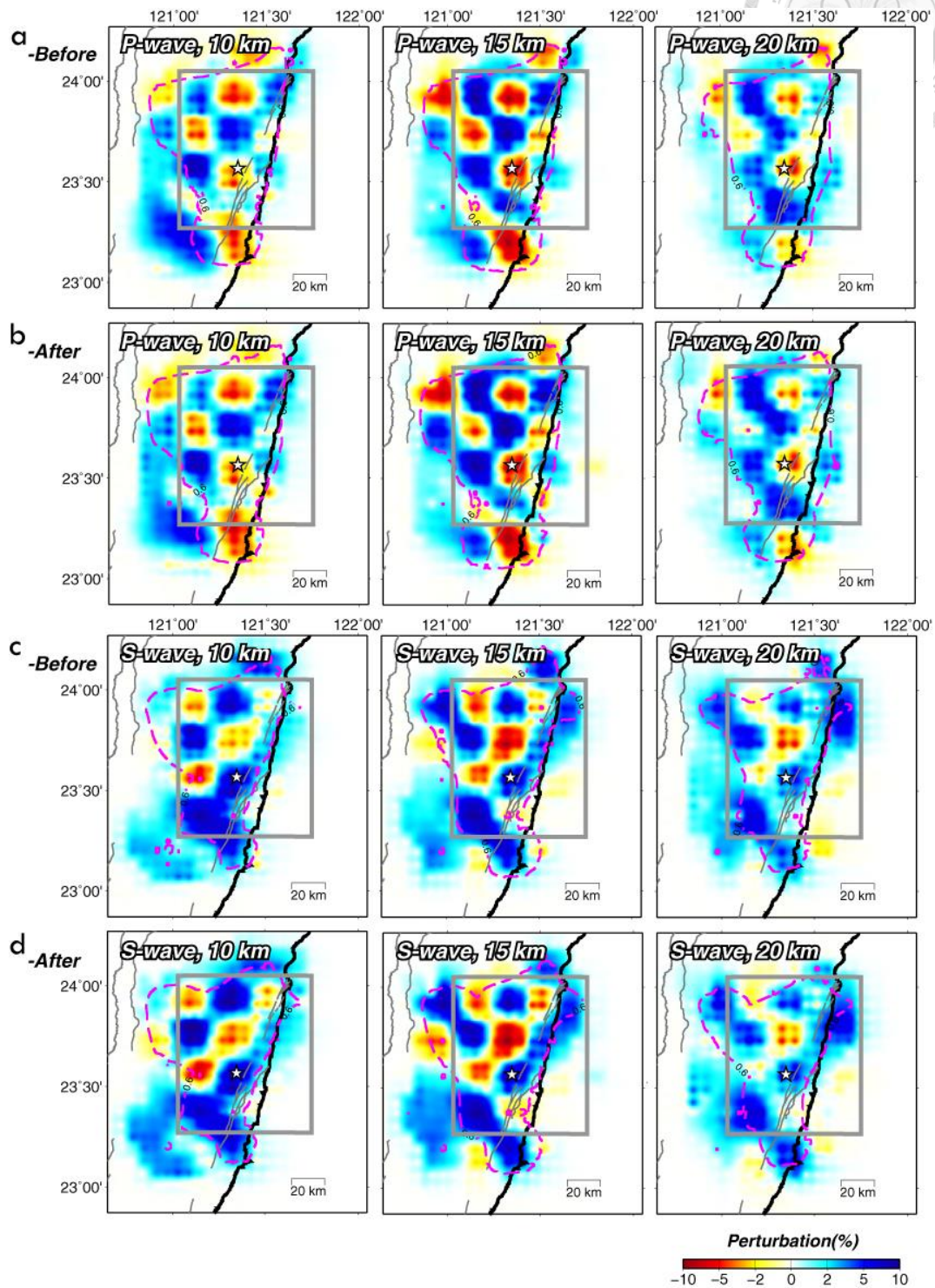
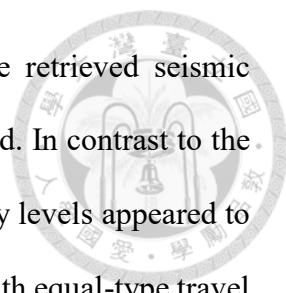


Figure 4.3 Recovered checkerboard-like models using equal-type travel time data (4000-arrivals) with travel time correction at 10, 15 and 20 km depth in two time periods before and after the 2013 Rueisuei earthquake. (a-d) see figure caption in Figure 4.1



With different recovery levels between two time periods, the retrieved seismic velocity changes from structures of two time periods would be biased. In contrast to the results inverted with unequal-type travel time data, the same recovery levels appeared to be in vicinity of the source region shown in the results of inverting with equal-type travel time data both of which without and with station corrections (Figures 4.4 and 4.5) and some dV anomalies had decreasing in intensity of anomalies when the travel time data were corrected, which clearly shown in the vertical sections (Figures 4.6 and 4.7).

4.3 Summary

The results of checkerboard resolution tests with different types of datasets indicate that not only will the distribution of rays influence the results of time-dependent travel time tomographic inversion but different weighting values of the arrival-pickings in travel time data also lead to artificial structures even though these rays are within the same paths in two time periods. The decreasing in intensity of dV anomalies are found to be accompanying with uniformly expanding resolvable region. Small dV anomalies around the source region give us a confidence in explanation of seismic velocity changes from our time-dependent tomographic results.

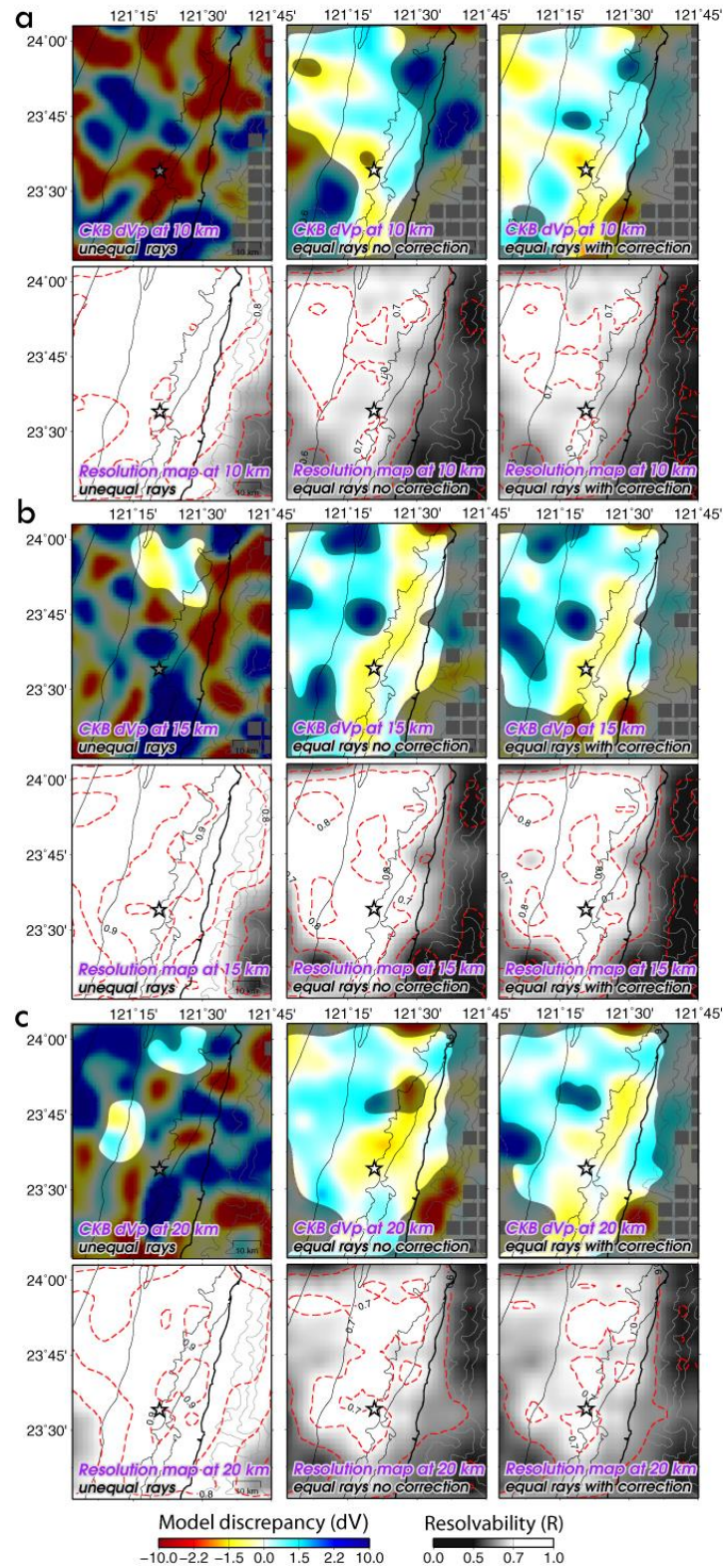


Figure 4.4 Discrepancy in resulting of checkerboard tests (dV) and resolution maps (R) in V_P and V_S using unequal-type travel time data, equal-type travel time data without station corrections and equal-type travel time data with station corrections between two time periods at (a) 10 km, (b) 15 km and (c) 20 km depth. White stars represent the epicenter of the 2013 Rueisuei mainshock. The region which have the dV value over of $\pm 1.5\%$

between two time periods and the R value less than 0.6 are shaded. Red dash lines in resolution maps show the R value with 0.1 in interval.

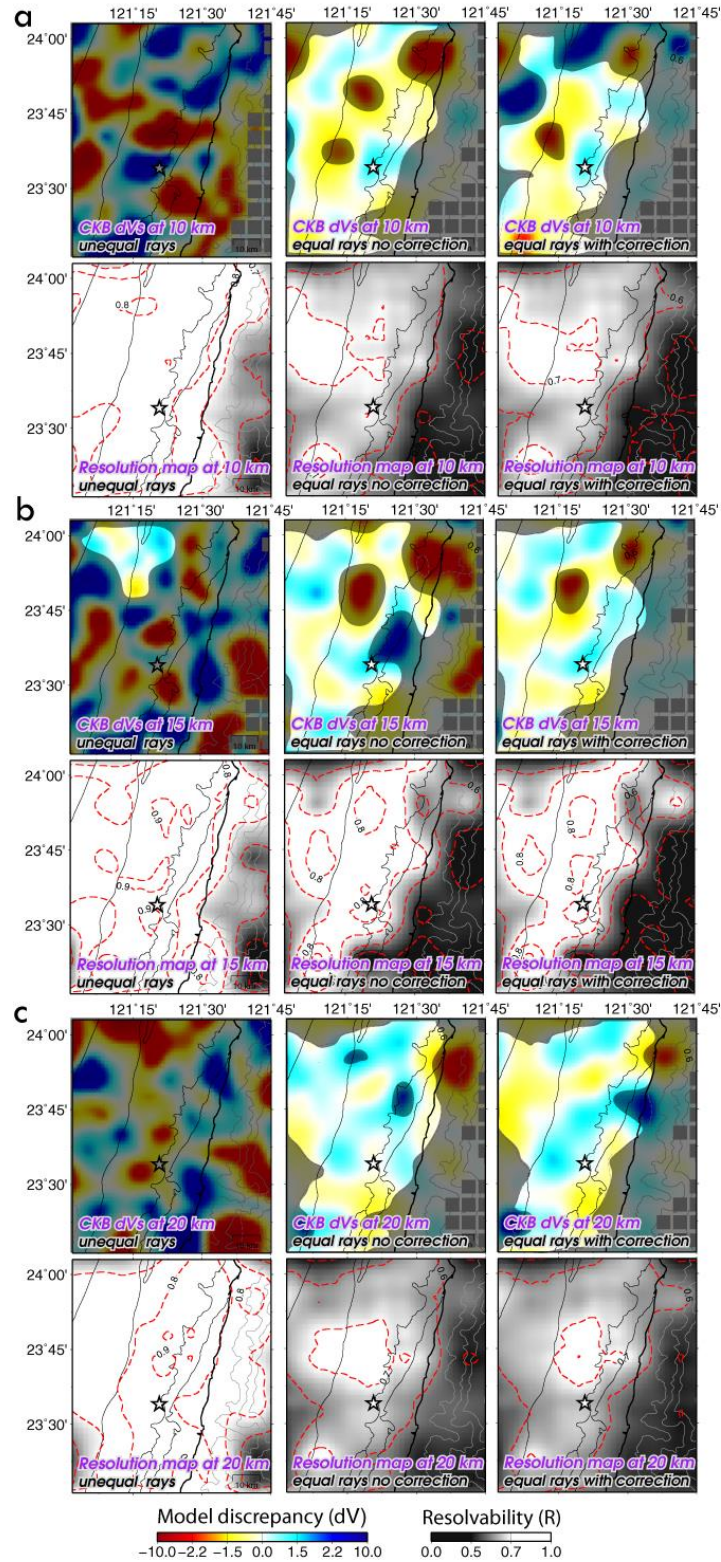
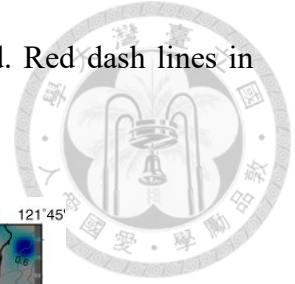


Figure 4.5 (Continued).

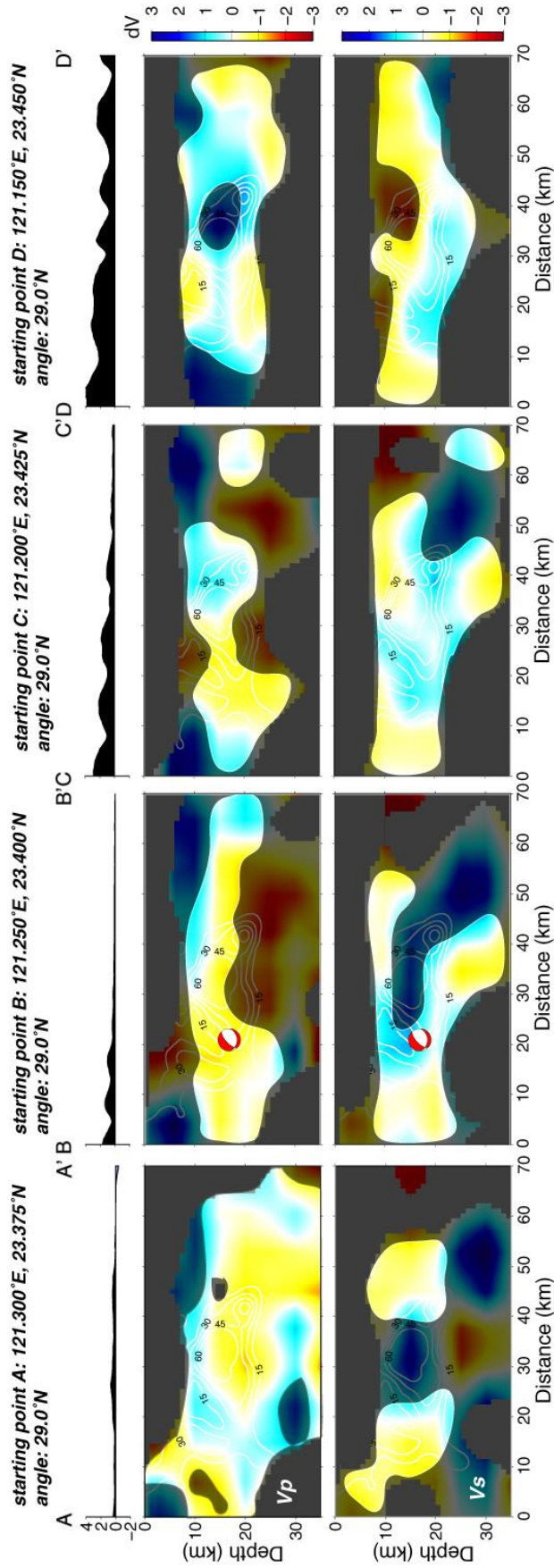


Figure 4.6 Checkerboard model discrepancy in V_P and V_S of vertical profile AA', BB', CC' and DD' along the track labeled in Figure 2.1(a) using equal-type travel time data without station corrections. The beach balls from the CWB CMT solution show the focal mechanism of the 2013 Rueisuei mainshock. Solid lines represent the major slip area of mainshock proposed by Lee et al. (2014).



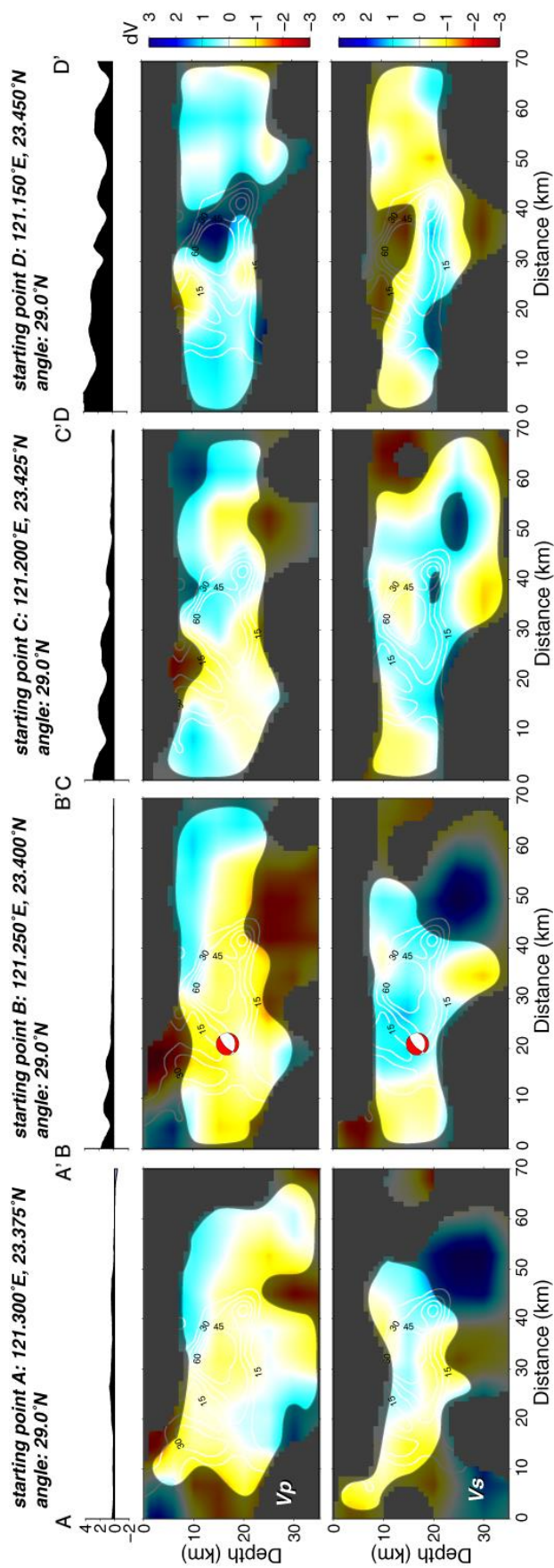
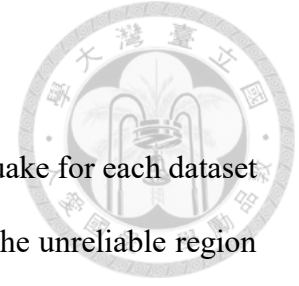


Figure 4.7 Checkerboard model discrepancy in V_p and V_s of vertical profiles AA', BB', CC' and DD' along the track labeled in Figure 2.1(a) using equal-type travel time data with station corrections. The beach balls from the CWB CMT solution show the focal mechanism of the 2013 Rueisuei mainshock. Solid lines represent the major slip area of mainshock proposed by Lee et al. (2014).



Chapter 5 Results and discussion



The ΔM in V_P and V_S before and after the 2013 Rueisuei earthquake for each dataset at 10, 15 and 20 km depth were shown in Figures 5.1 and 5.2 with the unreliable region being shaded. In the results of unequal-type travel time data, almost whole region had been shaded (Figures 5.1(a) and 5.2(a)), and it demonstrates how unequal ray distribution causes the artifacts in velocity structures. In contrast, the ΔM in the results of both two equal-type travel time data show very similar patterns and display a main tendency in the direction of north-east to south-west in velocity changes at all these three depth.

5.1 Model difference in V_P and V_S

For ΔM in V_P (Figure 5.1), a positive ΔM ($\sim 2\%$) was shown nearby the source location at 10 km depth and downwardly extended to encircle the source with a slightly increasing in intensity to $\sim 5\%$ at 15 km depth (Figure 5.1(c-1) and (c-2)). At 10 km depth, a negative ΔM ($\sim 3-8\%$) appeared in the north-eastern part of the source region and downwardly stretched to 15 km with decreasing in intensity ($\sim 1-2\%$). The aftershocks were mostly located at the high gradient changes in V_P around the source depth. Furthermore, at 20 km depth, a strong positive anomaly ($\sim 5-10\%$) was shown with a tendency in the NNE-SSW direction, which rupture of the fault plane propagated and where the following aftershocks occurred.

For ΔM in V_S (Figure 5.2) at 10 km depth, as same as ΔM in V_P , a negative ΔM ($\sim 5-10\%$) appeared in the north-eastern region of source location. Moreover, another negative ΔM ($\sim 5-10\%$) located at the west side of the source location and this anomaly downwardly extended to 15 km depth with decreasing in intensity to $\sim 3\%$. However, at 15 km depth, a strong positive anomaly ($\sim 5-10\%$) was shown with the same trending in

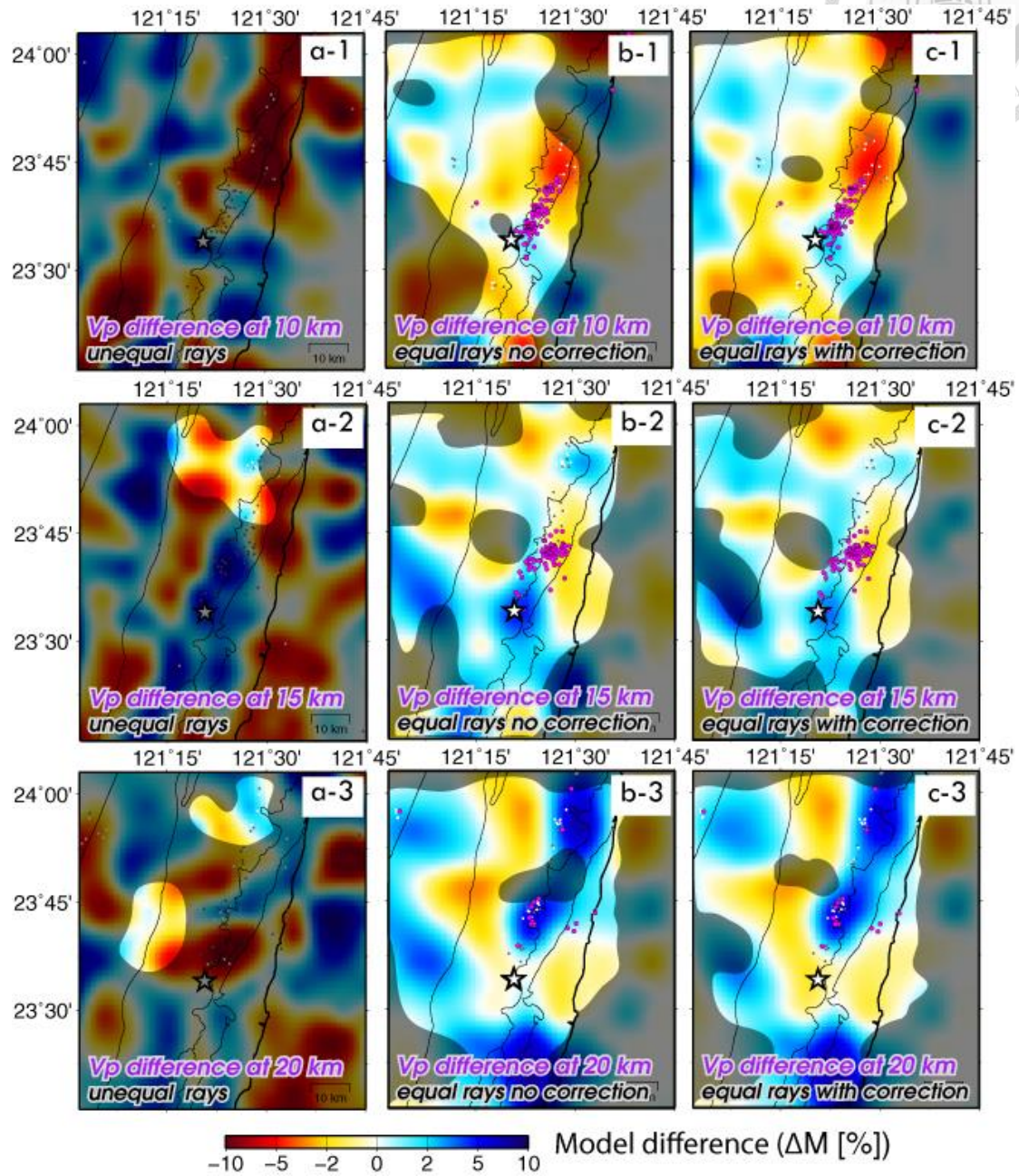


Figure 5.1 The model difference (ΔM) in V_P and V_S . (a) unequal-type travel time data, (b) equal-type travel time data without station corrections and (c) equal-type with station corrections in horizontal slices at 10、15、20 km depth with shaded unreliable region. White stars represent the epicenter of the 2013 Rueisuei mainshock. White dots and grey dots indicate the locations of input earthquakes projected on to the horizontal slice from 2.5 km each side before and after the 2013 Rueisuei mainshock and red dots represent the projected earthquakes occurred in following 10 days after the mainshock.

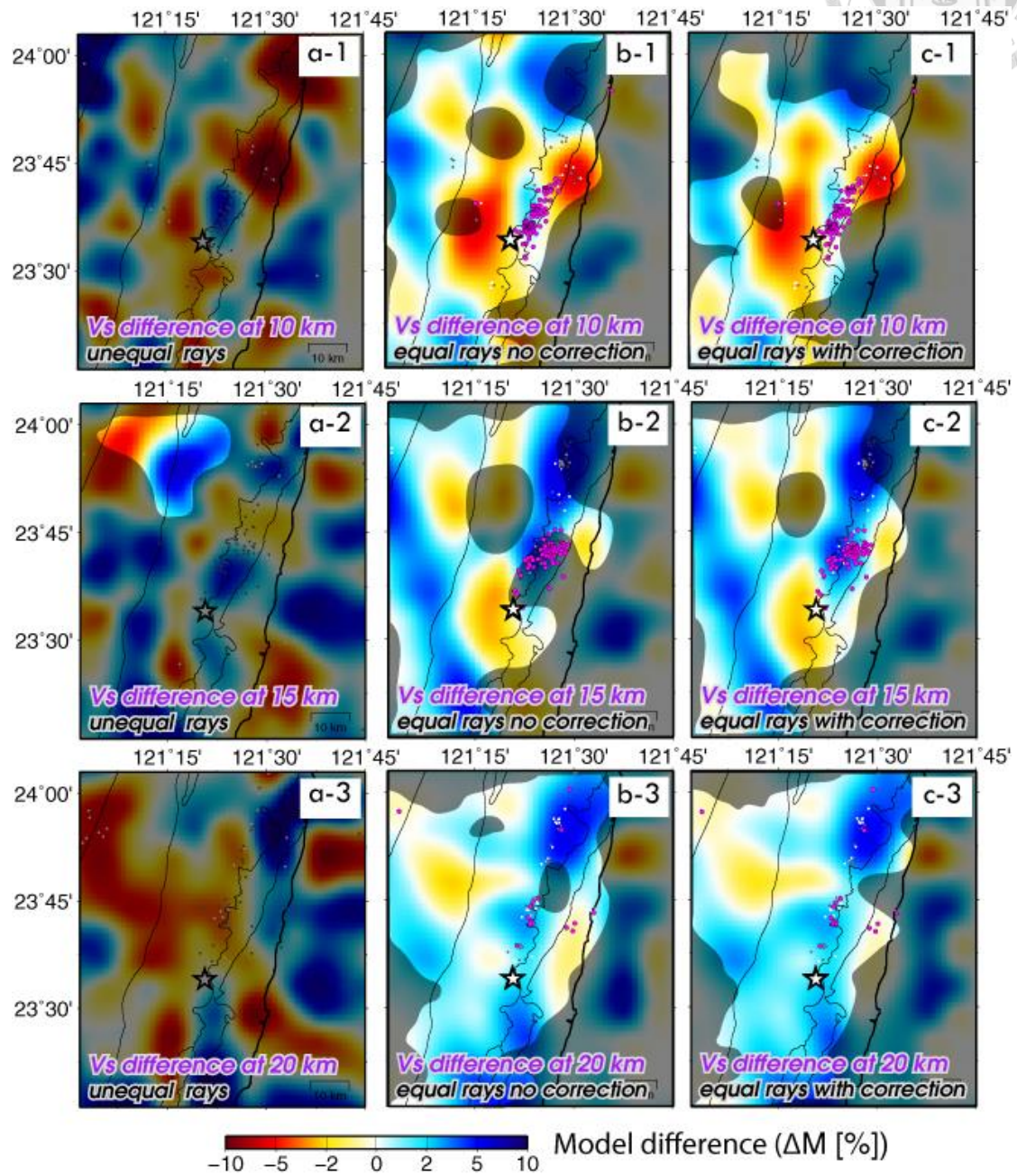
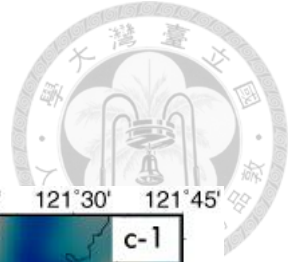
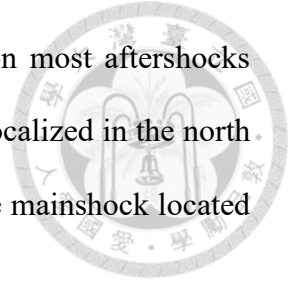


Figure 5.2 (Continued).

the NNE-SSW direction as ΔM in V_P at 20 km depth in the region most aftershocks occurred. This positive anomaly downwardly stretched and further localized in the north where is ~ 30 km away from the source location at 20 km depth. The mainshock located at high-gradient of changes in V_S .



5.2 Discussion

Previous studies (O'connell et al., 1974; Sibson et al., 1975; Winkler and Nur, 1979) have suggested that at the time of nucleation of an earthquake cracks and fractures are generated in stress dilatation zone. After the occurrence of earthquakes, migrating fluids can fill in these spaces and carry on material dissolved from the source rocks with not only a range of transported period of days to months but also a dimension from centimeter to kilometer (Sibson et al., 1975). The maximum change in velocity would be able to reach to on the order of 10-15%. Stress-induced changes of crack density have been considered to be one of major mechanisms causing variations in seismic velocities (Zhao et al., 1996; Chen et al., 2001; Vidale and Li, 2003; Chao and Peng, 2009; Taira et al., 2015). According to the hypothesis of stress-induced variations in seismic velocities, we compared our results of ΔM to the slip model on the fault plane (Lee et al., 2014; Figures 5.3 and 5.4, solid lines in vertical profiles which represent major slip area) and found that the positive changes in V_P (3-5%) and V_S (3-8%) taking place on the major slip area along the rupture direction to the north (vertical profile BB' in Figures 5.3 and 5.4). The negative anomalies located in the northern portion of major slip area at shallow depth from 8 to 15 km (vertical profiles AA', BB' and CC' in Figures 5.3 and 5.4). Most of the aftershocks were located on the boundary of the major slip area where there was high gradient change in V_P . Furthermore, another positive anomaly (~ 5 -10%) also appeared in the northern portion of

the major slip area where there was ~10-30 km away from source location at around 20 km depth. In addition, the positive change in V_S (~5-10%), which located at major slip area along the direction of rupture (vertical profiles BB' and CC' in Figures 5.3 and 5.4), also localized in the northern portion of the major slip area.

During the occurrence of earthquakes, energy is releasing from rapid slipping of the fault plane especially on asperities which dominantly causing the stress changes. In general, aftershocks will occur in following days after the mainshock to re-arrange the stress. Owing to the re-arrangement of the stress field, cracks could be either closure or opening and the seismic velocities must be perturbed (Nur 1971, Schaff and Beroza, 2004). Moreover, changes of stress are not only in the vicinity of source region but several kilometers away from the rupture zones (Vidale and Li, 2003). The stress concentrates on the boundary of the rupture area and the increasing stress in the region where has been compressed will respond to the positive changes in seismic velocities. On the contrary, in the opposite direction of rupture, the velocity will decrease because of extension.

The Philippine Sea Plate moved north-north-westward to obliquely collide with the Eurasian Plate. The CMT solution of the 2013 Rueisuei earthquake indicated a high-angle thrust focal mechanism with some left-lateral movement along the similar strike of the Longitudinal Valley, the onland suture between the Philippine Sea Plate and the Eurasian Plate. Considering the plate tectonic setting in eastern Taiwan and the numerical earthquake model proposed by Lee et al. (2014), we suggested the main cause of the velocity changes was due to the elastic rebound of the down-going foot wall block. Figure 5.5 illustrates the image of our interpretation. In the pre-seismic time period, the fault was locked. Some cracks were generated in the dilatation zone and the locked block was deformed at the same time. Since the mainshock occurred, the locked foot wall block rebounded downdip to the north (the white arrow in Figure 5.5) and so that the stress in

the northern region of the source location had been increased. Therefore, the positive changes in V_P and V_S were in the northern portion of major slip area and the northern region around the end of rupture due to the compression of crust. On the other hand, the regions in the opposite direction of rupture were extension in order that the velocities were decreased in those region. Therefore, these behaviors directly lead to variations in velocity structure after the occurrences of earthquakes. In this way, we suggested that the observed ΔM around the source region indicated the changes in stress due to the rupture of the mainshock and elastic rebound of the pre-locked block.

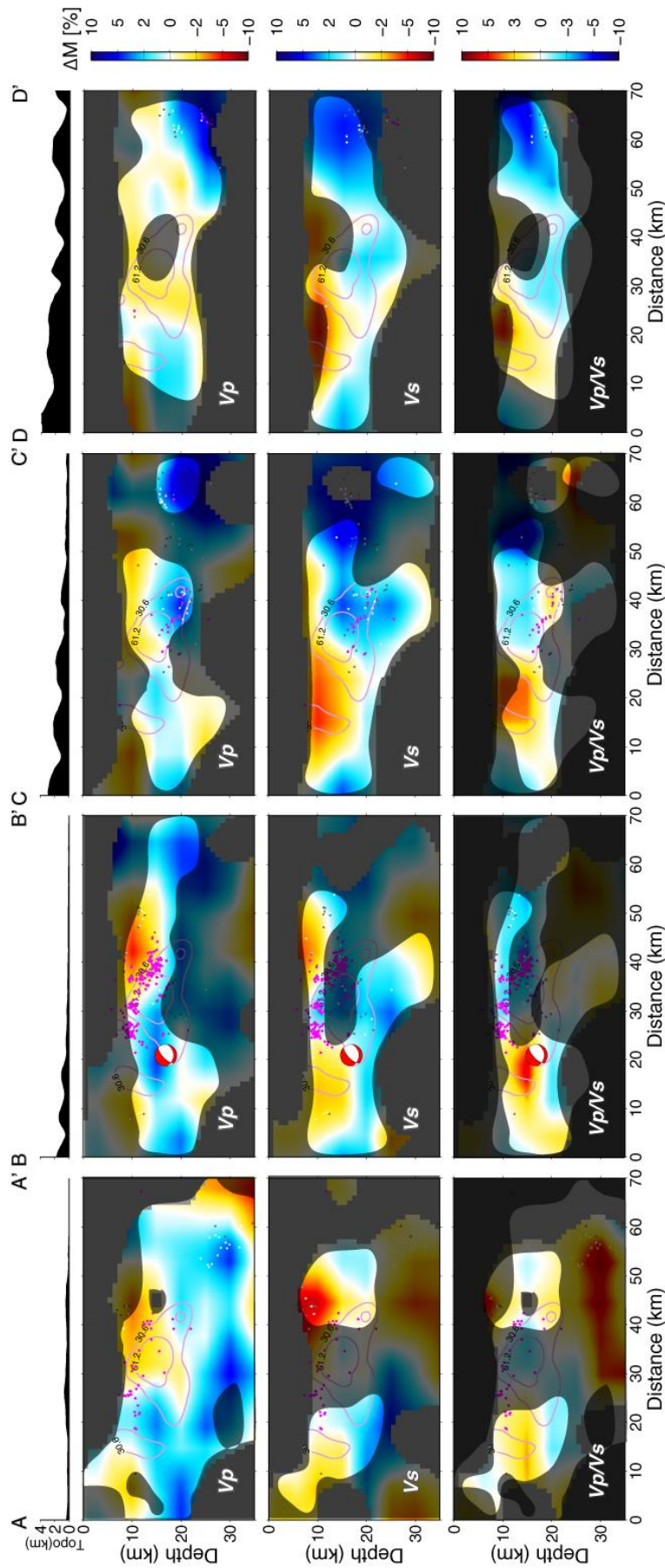


Figure 5.3 The model differences in V_p , V_s and V_p/V_s of vertical profile AA', BB', CC' and DD' along the track labeled in Figure 2.1(a) using equal-type travel time data without travel time correction. The beach balls from the CWB CMT solution show the focal mechanism of the 2013 Rueisuei mainshock. White and grey dots indicate the locations of input earthquakes projected on to the profile from 3 km each side before and after the 2013 Rueisuei mainshock and red dots represent the projected earthquakes occurred in following 10 days after the mainshock. Solid lines represent the major slip area of mainshock proposed by Lee et al. (2014).



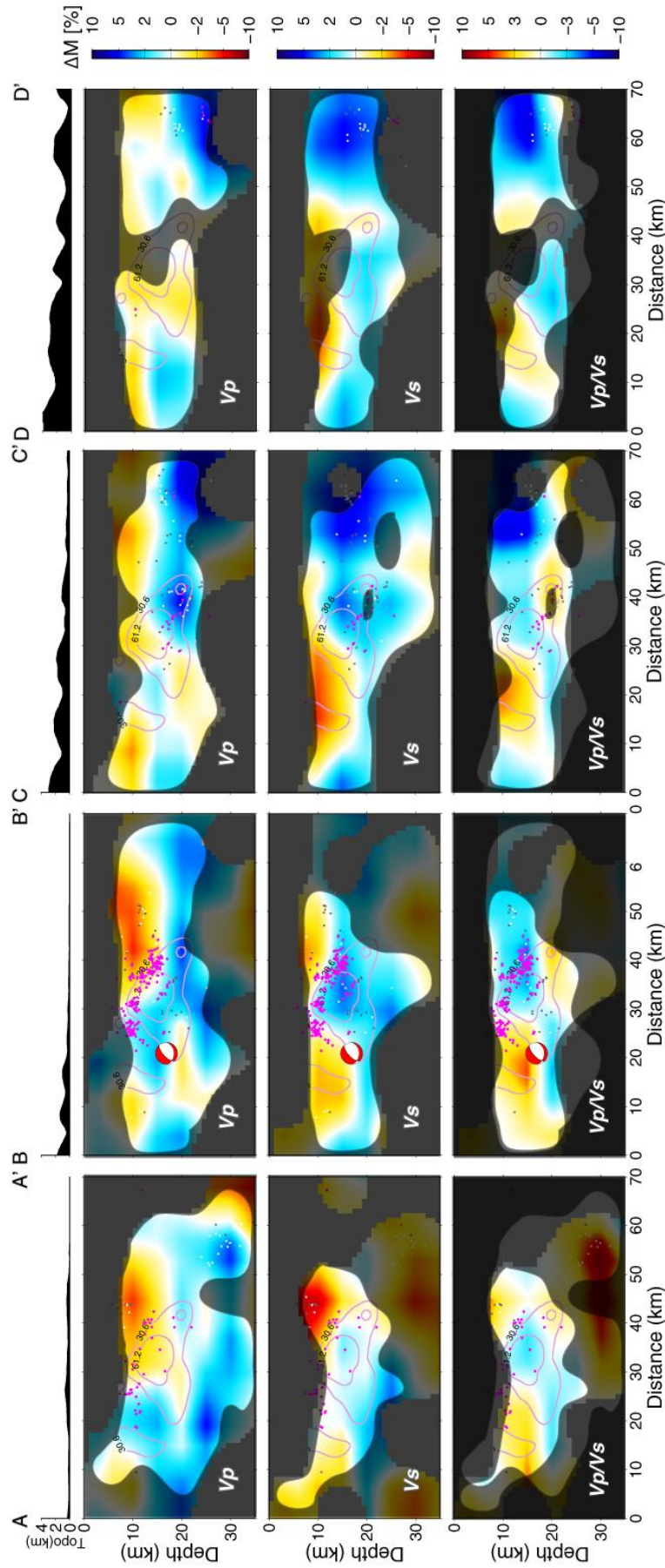


Figure 5.4 The model differences in V_p , V_s and V_p/V_s of vertical profile AA', BB', CC' and DD' along the track labeled in Figure 2.1(a) using equal-type travel time data with travel time correction. The beach balls from the CWB CMT solution show the focal mechanism of the 2013 Rueisuei mainshock. White and grey dots indicate the locations of input earthquakes projected on to the profile from 3 km each side before and after the 2013 Rueisuei mainshock. Red dots represent the projected earthquakes occurred in following 10 days after the mainshock. Solid lines represent the major slip area of mainshock proposed by Lee et al. (2014).

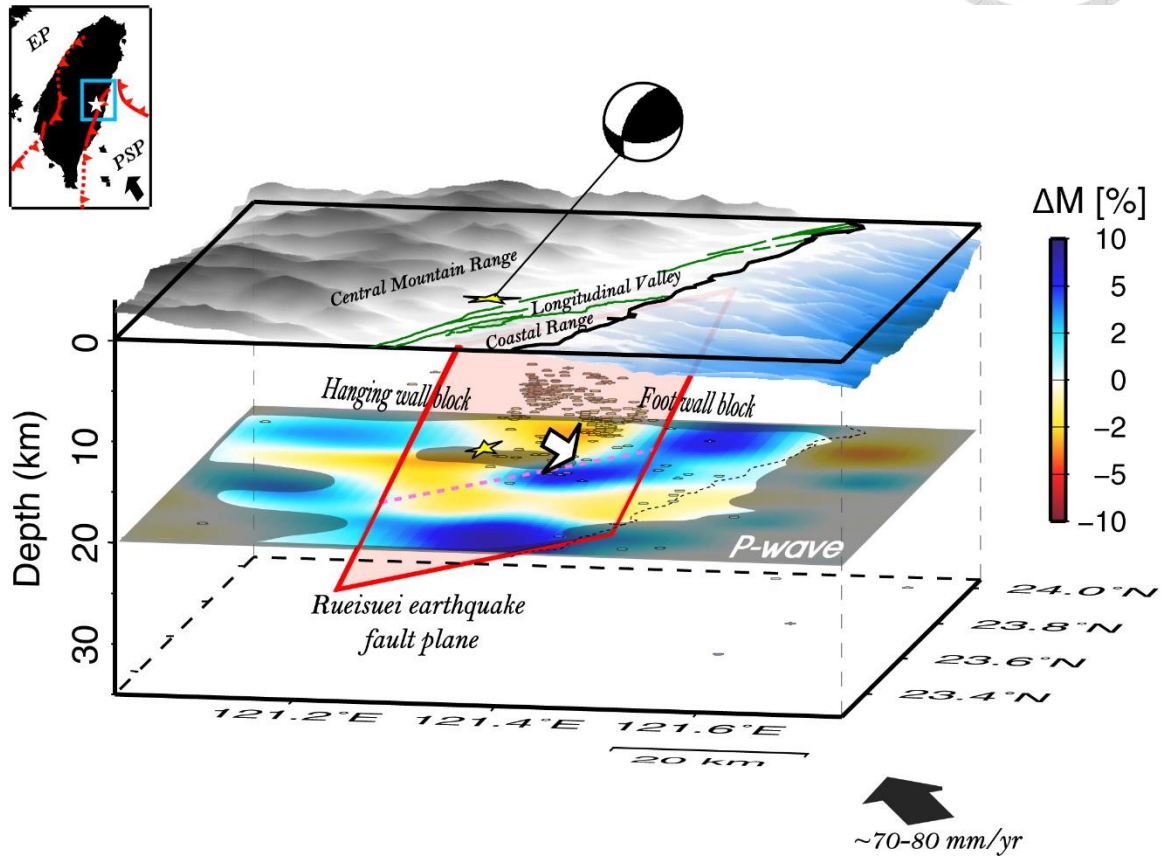


Figure 5.5 A perspective view of the fault plane of the 2013 Rueisuei earthquake in the northern Longitudinal Valley with the velocity changes (P -wave at 20 km depth) and the aftershocks distribution (circles). The fault plane was proposed by Lee et al. (2014). The yellow stars and the beach ball represent the hypocenter, epicenter and the CMT solution of the mainshock, respectively. Active faults are shown with green lines. The black arrow indicates the convergence rate of the Philippine Sea Plate (PSP) toward the Eurasian Plate (EP). The white arrow represents the downdip direction of the rebounded foot wall block.

Chapter 6 Conclusions

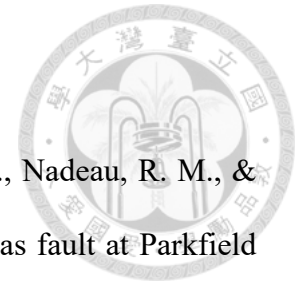


Real changes of material properties in Earth can be revealed by using repeated travel time tomographic inversion with equal ray distribution in different time periods based on the selection criteria of travel time data. In this study, we set up the location distance of each event pair to be 0.03° , the differences of epicentral distance to be 4 km and the gap of azimuths for each station-source pair to be 2° to sort out three types of datasets, including unequal-type, equal-type without station corrections and equal-type with station corrections in travel time data for examining the influence of ray distribution on tomographic results. Based on the checkerboard resolution tests, resolution maps and discrepancy between checkerboard-like models within two time periods, we found that the region with different recovery levels could be further reduced when the travel time data were corrected.

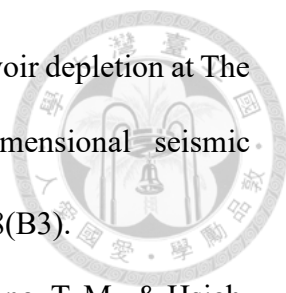
To conclude, in source region of the 2013 Rueisuei earthquake, a positive ΔM ($\sim 2\%$) in V_P was shown nearby the source location at 10 km depth and downwardly extended to encircle the source with slightly increasing in intensity to $\sim 5\%$ at 15 km depth. This anomaly downward and northward extended to ~ 10 -30 km away from the source location at 20 km depth with a tendency in the NNE-SSW direction, which the rupture of the fault plane propagated. In the north-eastern region of where the aftershocks distributed, a negative ΔM (~ 3 -8%) appeared at 10 km depth and downwardly stretched to 15 km with decreasing in intensity (~ 1 -2%). For ΔM in V_S , two negative ΔM (~ 5 -10%) appeared in the north-eastern region and the west side of the source location, and these anomalies downwardly extended to 15 km depth with decreasing in intensity to $\sim 3\%$. In the region where most aftershocks located, a strong positive anomaly (~ 5 -10%) was shown with the same trending in the NNE-SSW direction just located at the major slip area. This anomaly

downwardly stretched and further localized in the north where there was ~ 30 km away from the source location at 20 km depth. We suggested that the observed ΔM in the source region were mainly caused by increasing in stress due to the rupture of the mainshock and elastic rebound of crust. However, more efforts are needed for further understanding the mechanism of seismic velocity changes after occurrences of moderate-to-large earthquakes. The notable observation in this study is that not only will the distribution of rays affect the results of time-dependent travel time tomographic inversion but also different weighting values of the arrival-pickings in travel time data will bias the structures in tomographic inversion procedure. In addition, in order to sort out the equal ray distributions within different time periods, the seismic events should stably occur in the study area. When the comparable resolution of the two velocity images can be achieved, the travel time tomographic method could be a good means to help spatially delineate the changes in seismic velocities occur associated with the moderate-to-large sized earthquakes.

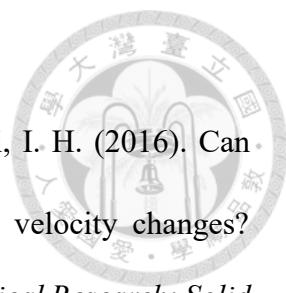
References

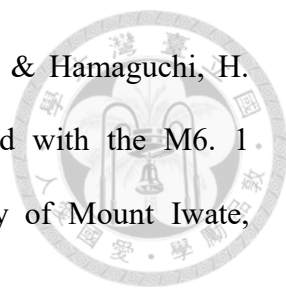


- [1] Brenguier, F., Campillo, M., Hadziioannou, C., Shapiro, N. M., Nadeau, R. M., & Larose, E. (2008). Postseismic relaxation along the San Andreas fault at Parkfield from continuous seismological observations. *Science*, 321(5895), 1478-1481.
- [2] Boore, D. M., Lindh, A. G., McEvilly, T. V., & Tolmachoff, W. W. (1975). A search for travel-time changes associated with the Parkfield, California, earthquake of 1966. *Bulletin of the Seismological Society of America*, 65(5), 1407-1418.
- [3] Chao, K., & Peng, Z. (2009). Temporal changes of seismic velocity and anisotropy in the shallow crust induced by the 1999 October 22 M6.4 Chia-Yi, Taiwan earthquake. *Geophysical Journal International*, 179(3), 1800-1816.
- [4] Chen, C. H., Wang, W. H., & Teng, T. L. (2001). 3D velocity structure around the source area of the 1999 Chi-Chi, Taiwan, earthquake: before and after the mainshock. *Bulletin of the Seismological Society of America*, 91(5), 1013-1027.
- [5] Chen, K. H., Furumura, T., Rubinstein, J., & Rau, R. J. (2011). Observations of changes in waveform character induced by the 1999 Mw7. 6 Chi - Chi earthquake. *Geophysical Research Letters*, 38(23).
- [6] Cheng, W. B. (2000). Three-dimensional crustal structure around the source area of the 1999 Chi-Chi earthquake in Taiwan and its relation to the aftershock locations. *Terrestrial, Atmospheric and Oceanic Sciences*, 11(3), 643-660.
- [7] Foulger, G. R., Grant, C. C., Ross, A., & Julian, B. R. (1997). Industrially induced changes in Earth structure at The Geysers geothermal area, California. *Geophysical research letters*, 24(2), 135-137.
- [8] Frohlich, C. (1979). An efficient method for joint hypocenter determination for large groups of earthquakes. *Computers & Geosciences*, 5(3), 387-389.


- 
- [9] Gunasekera, R. C., Foulger, G. R., & Julian, B. R. (2003). Reservoir depletion at The Geysers geothermal area, California, shown by four – dimensional seismic tomography. *Journal of Geophysical Research: Solid Earth*, 108(B3).
- [10] Huang, H. H., Wu, Y. M., Song, X., Chang, C. H., Lee, S. J., Chang, T. M., & Hsieh, H. H. (2014). Joint Vp and Vs tomography of Taiwan: Implications for subduction-collision orogeny. *Earth and Planetary Science Letters*, 392, 177-191.
- [11] Julian, B. R., & Foulger, G. R. (2010). Time-dependent seismic tomography. *Geophysical Journal International*, 182(3), 1327-1338.
- [12] Kanamori, H., & Fuis, G. (1976). Variation of P-wave velocity before and after the Galway Lake earthquake (ML= 5.2) and the Goat Mountain earthquakes (ML= 4.7, 4.7), 1975, in the Mojave desert, California. *Bulletin of the Seismological Society of America*, 66(6), 2017-2037.
- [13] Kao, H., Jian, P. R., Ma, K. F., Huang, B. S., & Liu, C. C. (1998). Moment-tensor inversion for offshore earthquakes east of Taiwan and their implications to regional collision. *Geophysical Research Letters*, 25(19), 3619-3622.
- [14] Kasatkina, E., Koulakov, I., West, M., & Izbekov, P. (2014). Seismic structure changes beneath Redoubt Volcano during the 2009 eruption inferred from local earthquake tomography. *Journal of Geophysical Research: Solid Earth*, 119(6), 4938-4954.
- [15] Kim, K. H., Chiu, J. M., Pujol, J., Chen, K. C., Huang, B. S., Yeh, Y. H., & Shen, P. (2005). Three-dimensional VP and VS structural models associated with the active subduction and collision tectonics in the Taiwan region. *Geophysical Journal International*, 162(1), 204-220.
- [16] Koketsu, K., & Sekine, S. (1998). Pseudo-bending method for three-dimensional seismic ray tracing in a spherical earth with discontinuities. *Geophysical Journal*

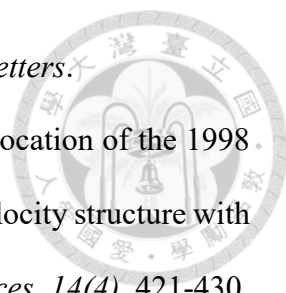
International, 132(2), 339-346.

- 
- [17] Koulakov, I., Gladkov, V., Khrepy, S. E., Al-Arifi, N., & Fathi, I. H. (2016). Can repeated passive source travel time tomography reveal weak velocity changes? Implications for the Tohoku region in Japan. *Journal of Geophysical Research: Solid Earth*.
- [18] Koulakov, I., Gordeev, E. I., Dobretsov, N. L., Vernikovsky, V. A., Senyukov, S., Jakovlev, A., & Jaxybulatov, K. (2013). Rapid changes in magma storage beneath the Klyuchevskoy group of volcanoes inferred from time-dependent seismic tomography. *Journal of Volcanology and Geothermal Research*, 263, 75-91.
- [19] Kuo-Chen, H., Wu, F. T., & Roecker, S. W. (2012). Three-dimensional P velocity structures of the lithosphere beneath Taiwan from the analysis of TAIGER and related seismic data sets. *Journal of Geophysical Research: Solid Earth* (1978–2012), 117(B6).
- [20] Lee, S. J., Huang, H. H., Shyu, J. B. H., Yeh, T. Y., & Lin, T. C. (2014). Numerical earthquake model of the 31 October 2013 Ruisui, Taiwan, earthquake: Source rupture process and seismic wave propagation. *Journal of Asian Earth Sciences*, 96, 374-385.
- [21] Lees, J. M., & Nicholson, C. (1993). Three-dimensional tomography of the 1992 southern California earthquake sequence: Constraints on dynamic earthquake rupture? *Geology*, 21(5), 387-390.
- [22] Liang, C., Song, X., & Huang, J. (2004). Tomographic inversion of Pn travel times in China. *Journal of Geophysical Research: Solid Earth* (1978–2012), 109(B11).
- [23] Ma, K. F., Wang, J. H., & Zhao, D. (1996). Three-Dimensional Seismic Velocity Structure of the Crust and Uppermost Mantle beneath Taiwan. *Journal of Physics of the Earth*, 44(2), 85-105.

- 
- [24] Nishimura, T., Uchida, N., Sato, H., Ohtake, M., Tanaka, S., & Hamaguchi, H. (2000). Temporal changes of the crustal structure associated with the M6. 1 earthquake on September 3, 1998, and the volcanic activity of Mount Iwate, Japan. *Geophys. Res. Lett*, 27(2), 269-272.
- [25] Nur, A. (1971). Effects of stress on velocity anisotropy in rocks with cracks. *Journal of Geophysical Research*, 76(8), 2022-2034.
- [26] O'Connell, R. J., & Budiansky, B. (1974). Seismic velocities in dry and saturated cracked solids. *Journal of Geophysical Research*, 79(35), 5412-5426.
- [27] Patanè, D., Barberi, G., Cocina, O., De Gori, P., & Chiarabba, C. (2006). Time-resolved seismic tomography detects magma intrusions at Mount Etna. *Science*, 313(5788), 821-823.
- [28] Peng, Z., & Ben-Zion, Y. (2006). Temporal changes of shallow seismic velocity around the Karadere-Düzce branch of the north Anatolian fault and strong ground motion. *Pure and Applied Geophysics*, 163(2-3), 567-600.
- [29] Poupinet, G., Ellsworth, W. L., & Frechet, J. (1984). Monitoring velocity variations in the crust using earthquake doublets: An application to the Calaveras Fault, California. *Journal of Geophysical Research: Solid Earth (1978–2012)*, 89(B7), 5719-5731.
- [30] Rau, R. J., & Wu, F. T. (1995). Tomographic imaging of lithospheric structures under Taiwan. *Earth and Planetary Science Letters*, 133(3), 517-532.
- [31] Schaff, D. P., & Beroza, G. C. (2004). Coseismic and postseismic velocity changes measured by repeating earthquakes. *Journal of Geophysical Research: Solid Earth*, 109(B10).
- [32] Shin, T. C. (1992). Some implications of Taiwan tectonic features from the data collected by the Central Weather Bureau Seismic Network. *Meteorol. Bull*, 38, 23-

48. (in Chinese)

- 
- [33] Shin, T. C. (1993, December). Progress summary of the Taiwan strong motion instrumentation program. In *Symp. on the Taiwan strong motion instrumentation program* (Vol. 1, No. 10). (in Chinese)
- [34] Shin, T. C., Tsai, Y. B., Yeh, Y. T., Liu, C. C., Wu, Y. M., (2003). Strong motion instrumentation programs in Taiwan, in *Handbook of Earthquake and Engineering Seismology*, W. H. K. Lee, H. Kanamori and P. C. Jennings (Editors), Academic Press, New York, 1057–1602.
- [35] Sibson, R. H., Moore, J. M. M., & Rankin, A. H. (1975). Seismic pumping—a hydrothermal fluid transport mechanism. *Journal of the Geological Society*, 131(6), 653-659.
- [36] Soldati, G., Zaccarelli, L., Faenza, L., & Michelini, A. (2015). Monitoring of crustal seismic velocity variations in the L'Aquila fault zone inferred from noise cross-correlation. *Geophysical Journal International*, 202(1), 604-611.
- [37] Taira, T. A., Brenguier, F., & Kong, Q. (2015). Ambient noise-based monitoring of seismic velocity changes associated with the 2014 Mw 6.0 South Napa earthquake. *Geophysical Research Letters*, 42(17), 6997-7004.
- [38] Um, J., & Thurber, C. (1987). A fast algorithm for two-point seismic ray tracing. *Bulletin of the Seismological Society of America*, 77(3), 972-986.
- [39] Vidale, J. E., & Li, Y. G. (2003). Damage to the shallow Landers fault from the nearby Hector Mine earthquake. *Nature*, 421(6922), 524-526.
- [40] Winkler, K., & Nur, A. (1979). Pore fluids and seismic attenuation in rocks. *Geophysical Research Letters*, 6(1), 1-4.
- [41] Wu, C., Delorey, A., Brenguier, F., Hadziioannou, C., Daub, E. G., & Johnson, P. (2016). Constraining depth range of S - wave velocity decrease after large

- 
- earthquakes near Parkfield, California. *Geophysical Research Letters*.
- [42] Wu, Y. M., Chang, C. H., Hsiao, N. C., & Wu, F. T. (2003). Relocation of the 1998 Rueyli, Taiwan, earthquake sequence using three-dimensions velocity structure with stations corrections. *Terrestrial Atmospheric and Oceanic Sciences*, 14(4), 421-430.
- [43] Wu, Y. M., Chang, C. H., Zhao, L., Shyu, J. B. H., Chen, Y. G., Sieh, K., & Avouac, J. P. (2007). Seismic tomography of Taiwan: Improved constraints from a dense network of strong motion stations. *Journal of Geophysical Research: Solid Earth* (1978–2012), 112(B8).
- [44] Wu, Y. M., Chang, C. H., Zhao, L., Teng, T. L., & Nakamura, M. (2008). A comprehensive relocation of earthquakes in Taiwan from 1991 to 2005. *Bulletin of the Seismological Society of America*, 98(3), 1471-1481.
- [45] Wu, Y. M., Shyu, J. B. H., Chang, C. H., Zhao, L., Nakamura, M., & Hsu, S. K. (2009). Improved seismic tomography offshore northeastern Taiwan: implications for subduction and collision processes between Taiwan and the southernmost Ryukyu. *Geophysical Journal International*, 178(2), 1042-1054.
- [46] Xu, Z. J., & Song, X. (2009). Temporal changes of surface wave velocity associated with major Sumatra earthquakes from ambient noise correlation. *Proceedings of the National Academy of Sciences*, 106(34), 14207-14212.
- [47] Yu, T. C., & Hung, S. H. (2012). Temporal changes of seismic velocity associated with the 2006 Mw 6.1 Taitung earthquake in an arc–continent collision suture zone. *Geophysical Research Letters*, 39(12).
- [48] Yu, W. C., Song, T. R. A., & Silver, P. G. (2013). Temporal velocity changes in the crust associated with the great Sumatra earthquakes. *Bulletin of the Seismological Society of America*, 103(5), 2797-2809.
- [49] Zelt, C. A. (1998). Lateral velocity resolution from three-dimensional seismic

refraction data. *Geophysical Journal International*, 135(3), 1101-1112.

- [50] Zhao, D., & Kanamori, H. (1995). The 1994 Northridge earthquake: 3-D crustal structure in the rupture zone and its relation to the aftershock locations and mechanisms. *Geophysical research letters*, 22(7), 763-766.
- [51] Zhao, D., Kanamori, H., Negishi, H., & Wiens, D. (1996). Tomography of the source area of the 1995 Kobe earthquake: evidence for fluids at the hypocenter? *Science*, 274(5294), 1891-1894.

Appendices

A. Initial 3-D velocity models for tomographic inversion

In inversion process, the initial velocity model is one of the dominant constraints on the results. For tomographic inversion, certainly, more stable and feasible results would be obtained through a realistic initial model especially using less travel time data.

Based on such considerations we changed the initial 1-D velocity model to 3-D models which inverted with an initial 1-D velocity model and travel time data of entire time periods including pre-seismic and post-seismic time periods of the mainshock, for repeated tomographic inversion described in Chapter 2. Here, we also conducted a number of tests to ensure the recovery abilities in each time period. Figures A1-A6 show the initial 3-D models for each type of travel time data and their results of checkerboard resolution tests at depth of 10, 15 and 20 km, respectively.

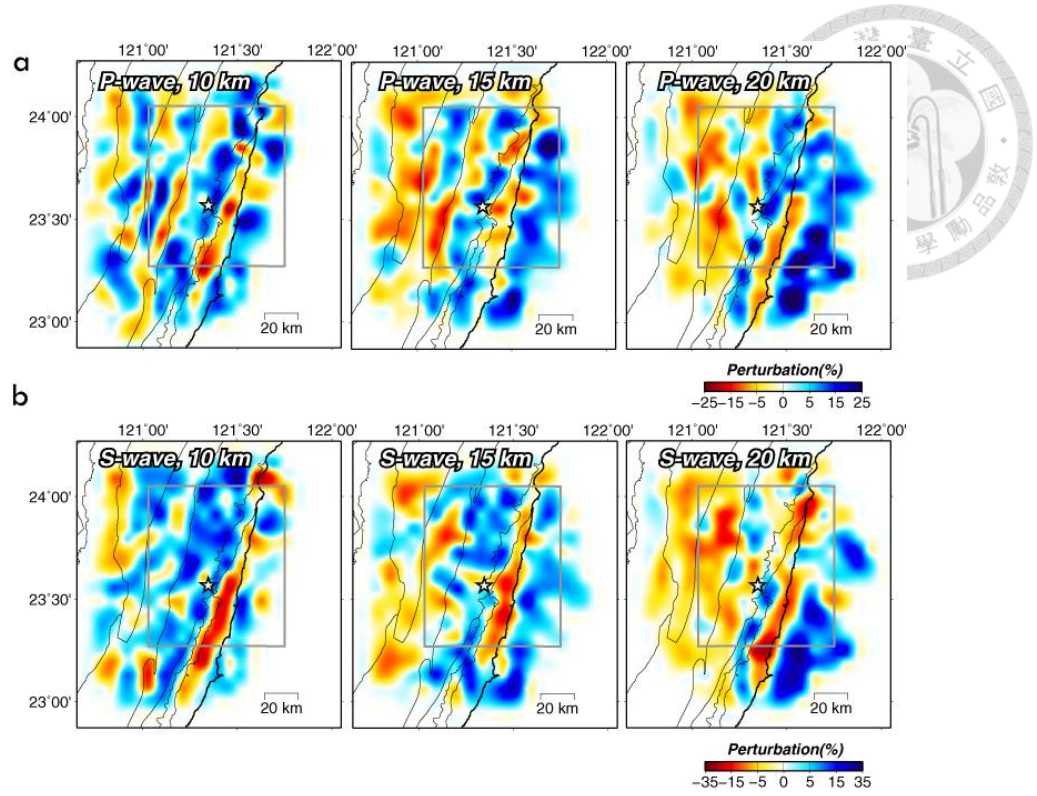


Figure A 1. The initial 3-D model of unequal-type travel time data.

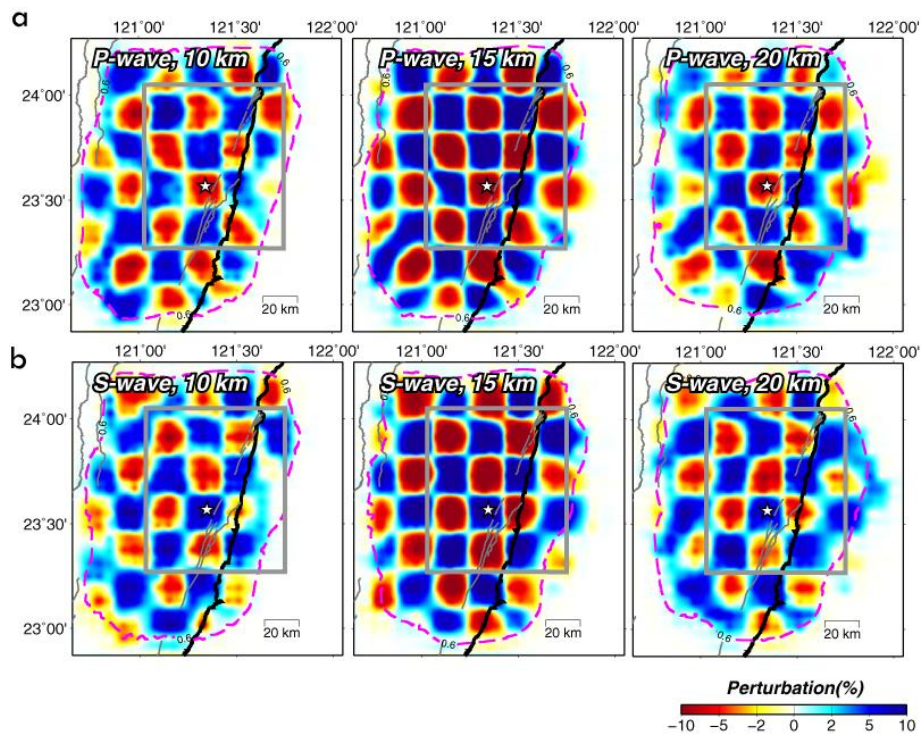


Figure A 2. Recovered checkerboard-like structure for the initial 3-D model of unequal-type travel time data.

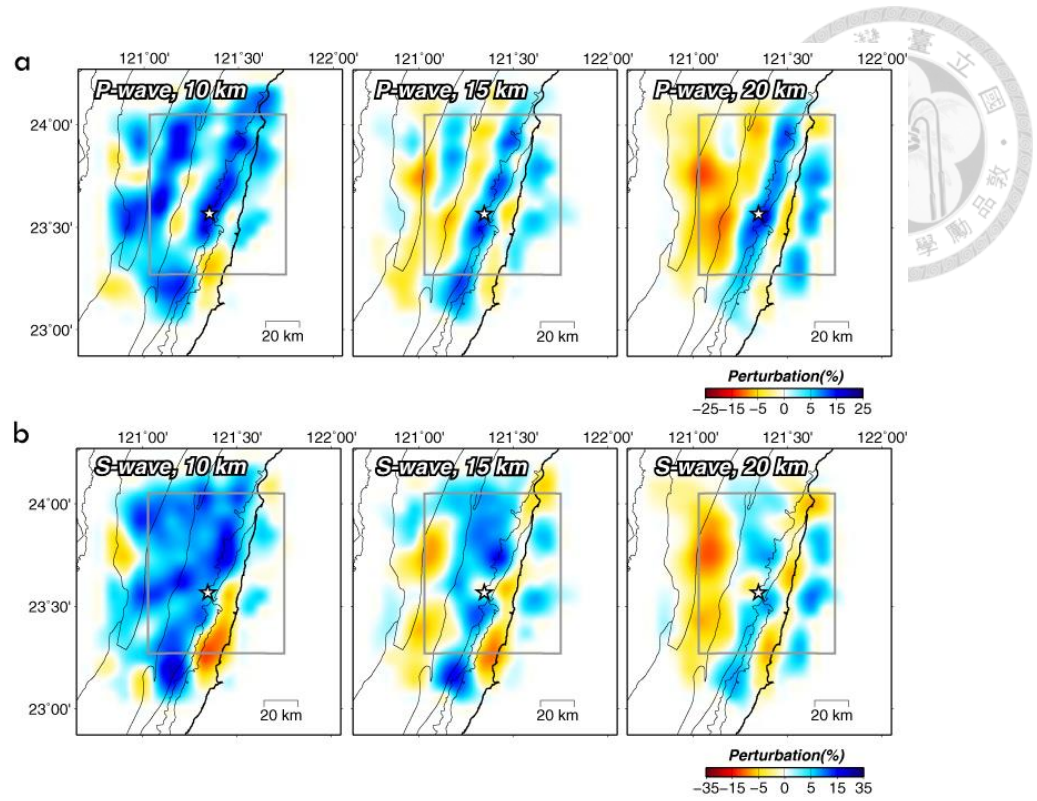


Figure A 3. The initial 3-D model of equal-type travel time data without station corrections.

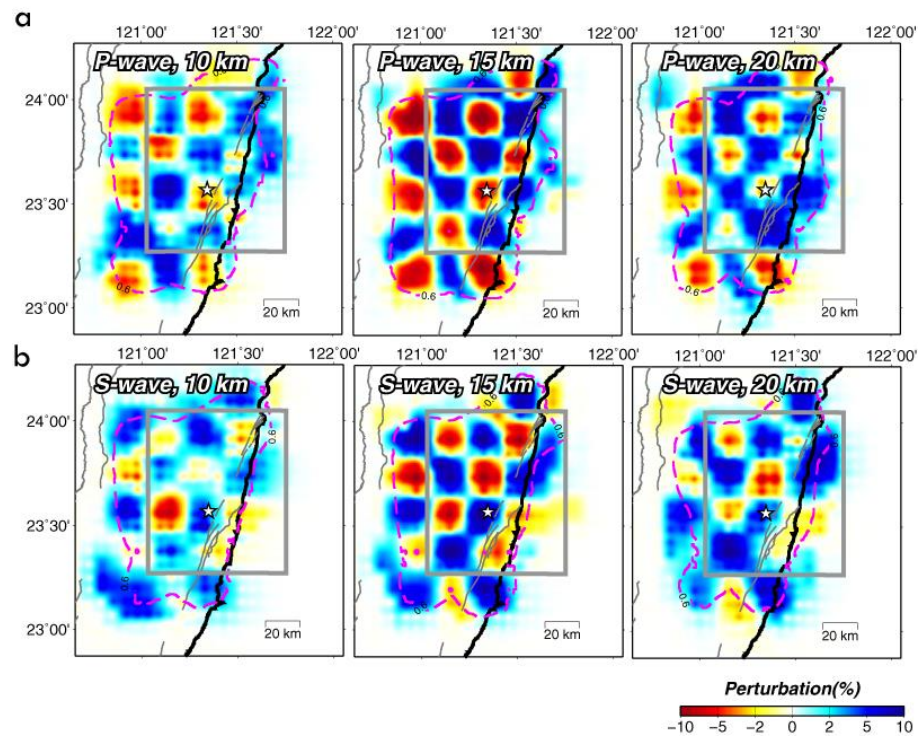


Figure A 4. Recovered checkerboard-like structure for the initial 3-D model of equal-type travel time data without station corrections.

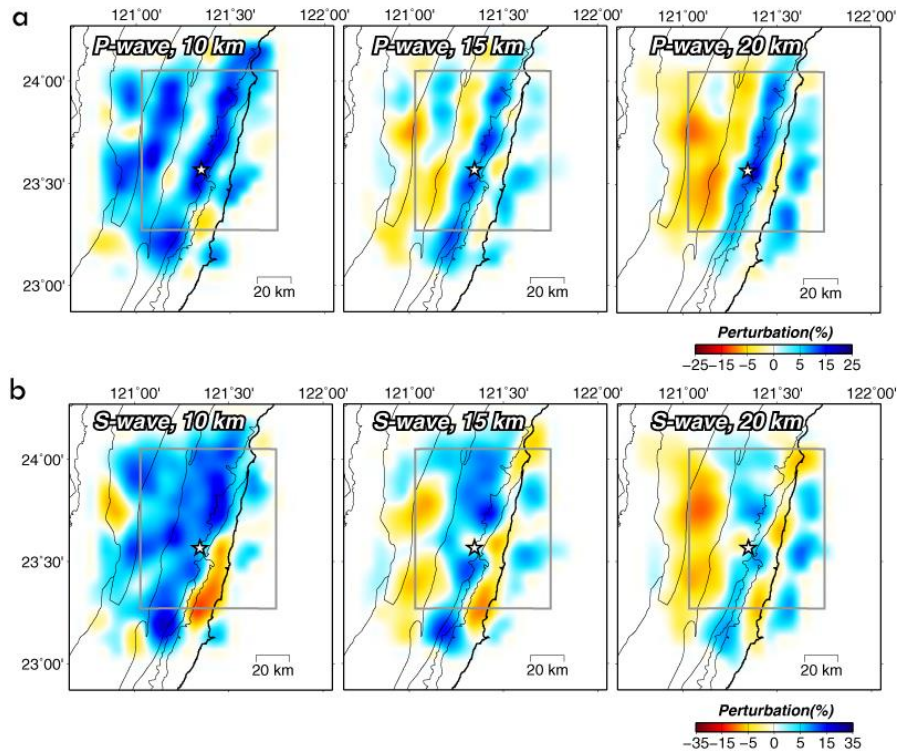


Figure A 5. The initial 3-D model of equal-type travel time data with station corrections.

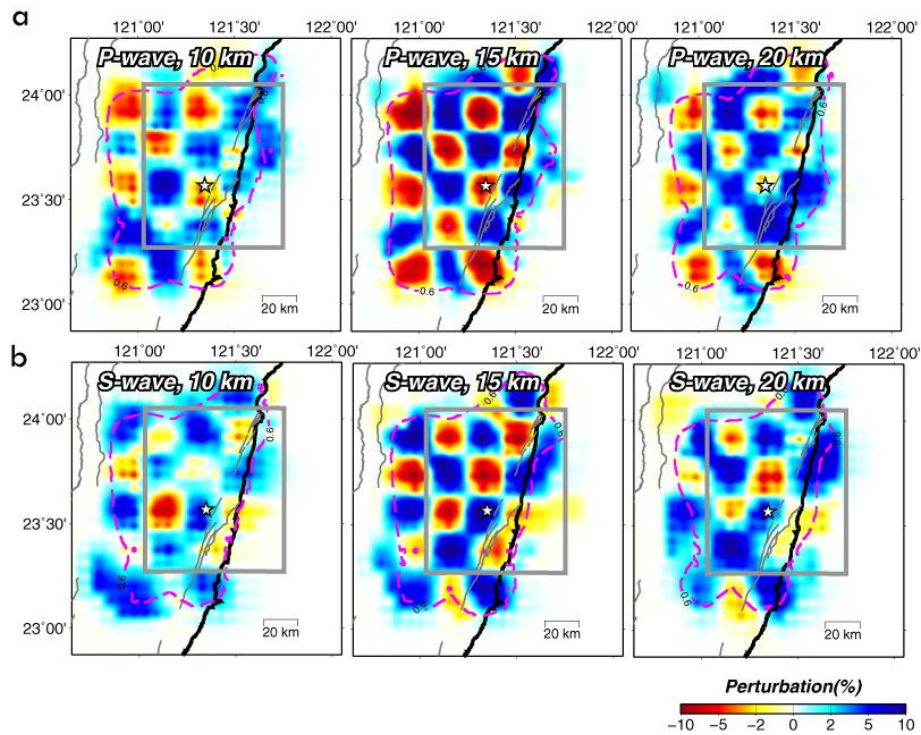


Figure A 6. Recovered checkerboard-like structure for the initial 3-D model of equal-type travel time data with station corrections.

B. Testing for different value of smoothing and damping factors



Except for the initial model, the value of smoothing and damping factors also play a critical role in what we can see through the inversion procedure. Value of smoothing factor dominantly limit the adjustment in scales over the model space and value of damping factor dominantly constrain the degree of fitting of data.

Here, different values of smoothing and damping factors were tested for tomographic inversion with equal-type travel time data without station corrections to demonstrate how these two factors constrain the inversions. Figures B1 and B2 represent the results of ΔM with fixing the value of damping factor to be 30 and changing the smoothing value to be 10 and 50. In Figure B1, some small anomalies were retrieved in results of ΔM and some strong anomalies were appeared on the boundary of study area due to a smaller value of smoothing factor. However, because of a larger value of smoothing factor used in tomographic inversion Figure B2 shows quite smooth structure in results of ΔM rather than Figure B1. Figures B3 and B4 represent the results of ΔM with fixing the value of smoothing factor to be 20 and changing the damping value to be 15 and 50. In Figure B3, most anomalies were retrieved in results of ΔM with strong amplitude due to a smaller value of damping factor. However, when the value of damping factor increased, these amplitude of anomalies became weaker.

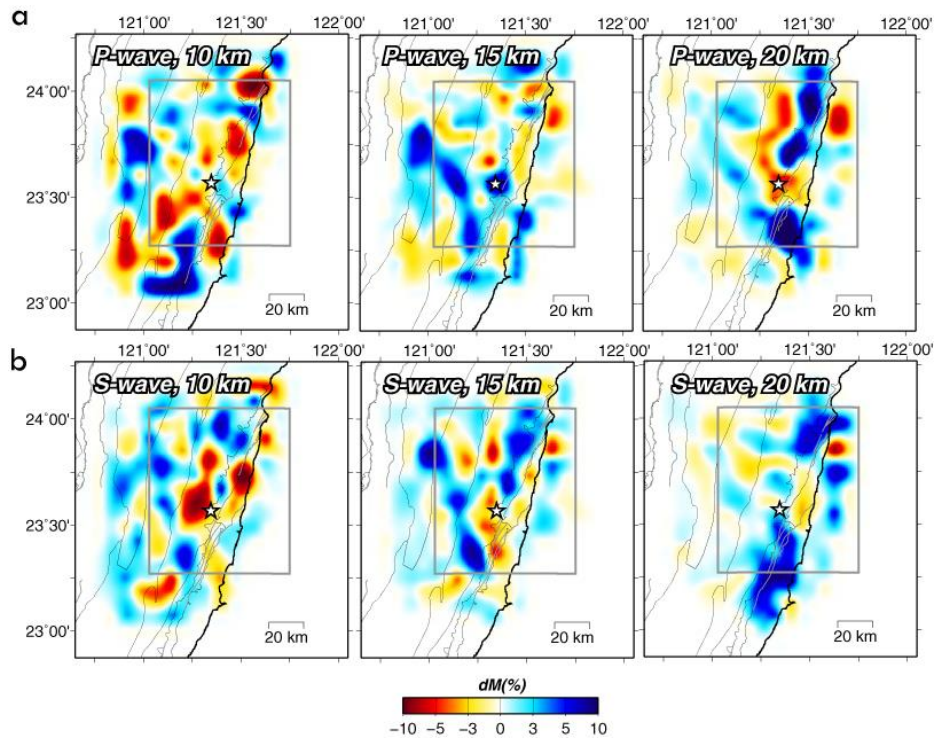


Figure B 1. The results of ΔM using the initial 3-D model, equal-type travel time data without station corrections. The value of smoothing and damping factors were chosen to be 10 and 30 (Figure 3.3 (b)), respectively.

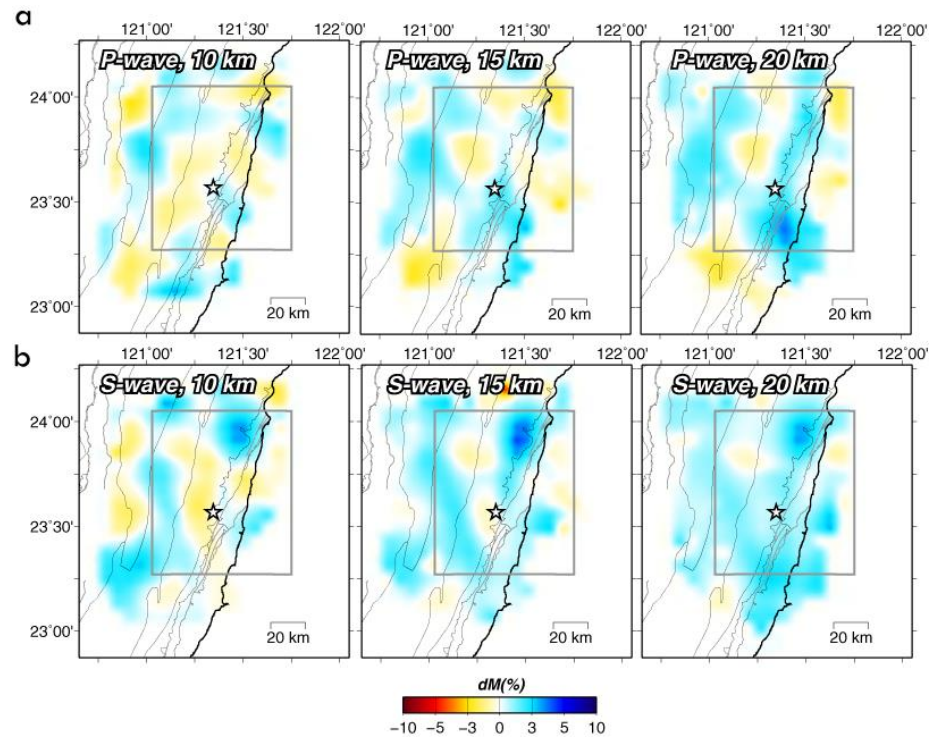


Figure B 2. The results of ΔM using the initial 3-D model, equal-type travel time data without station corrections. The value of smoothing and damping factors were chosen to be 50 and 30 (Figure 3.3 (b)), respectively.

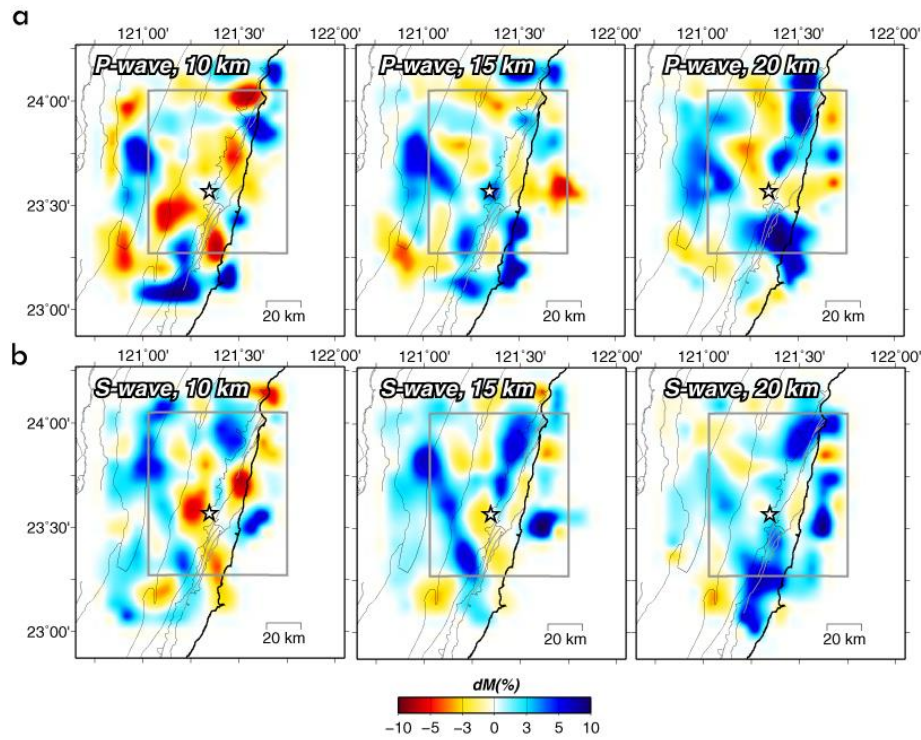


Figure B 3. The results of ΔM using the initial 3-D model, equal-type travel time data without station corrections. The value of smoothing and damping factors were chosen to be 20 and 15 (Figure 3.3 (b)), respectively.

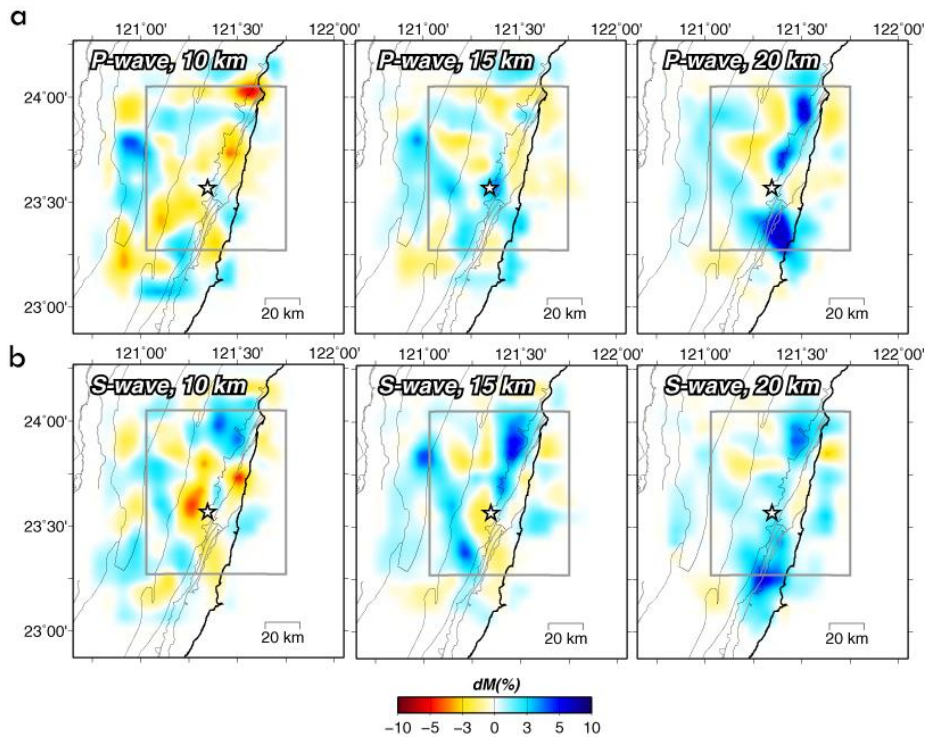


Figure B 4. The results of ΔM using the initial 3-D model, equal-type travel time data without station corrections. The value of smoothing and damping factors were chosen to be 20 and 50 (Figure 3.3 (b)), respectively.

C. Time-expending tomographic inversion

Testing of repeating tomography to find temporal-spatial velocity change in crust, we sort out 4000-*arrivals* from relocated earthquake catalog based on the selection criteria of equal-type travel time data in ray distribution before and after the mainshock, which described in Chapter 2. Then overlapped adding travel time data from 3200 to 4000 to represent extending over time. The V_P and V_S structures were obtained through the regional travel time tomography algorithm proposed by Huang et al. (2014) with the initial 3-D velocity structure which were retrieved from inverting with travel time data of entire time periods, and 15 iterations were executed without updated event locations. In order to examine the reliability of resolvable region, we also conducted checkerboard resolution tests, resolution maps and discrepancy of checkerboard-like models.

The ΔM before and after the 2013 Rueisuei earthquake of each dataset at 10, 15 and 20 km depth were shown in Figures C1, C2 and C3 with the shaded unreliable region. Similar to the results of dV the anomalies become localized with the systematically increasing in travel time data. In a comprehensive consideration of the results of R value and dV between two time periods, 3200-*arrivals* seem insufficient to obtain a well recovered structure from tomographic inversion. However, the patterns of dV have similar trend with the dV results using 3600 to 4000-*arrivals*. With systematically increasing in travel time data from 3600 to 4000-*arrivals*, these anomalies become localized and have a decreasing in the intensity of anomaly. As expected, the best resolvable region appears in the results of inverting with 4000-*arrivals*.

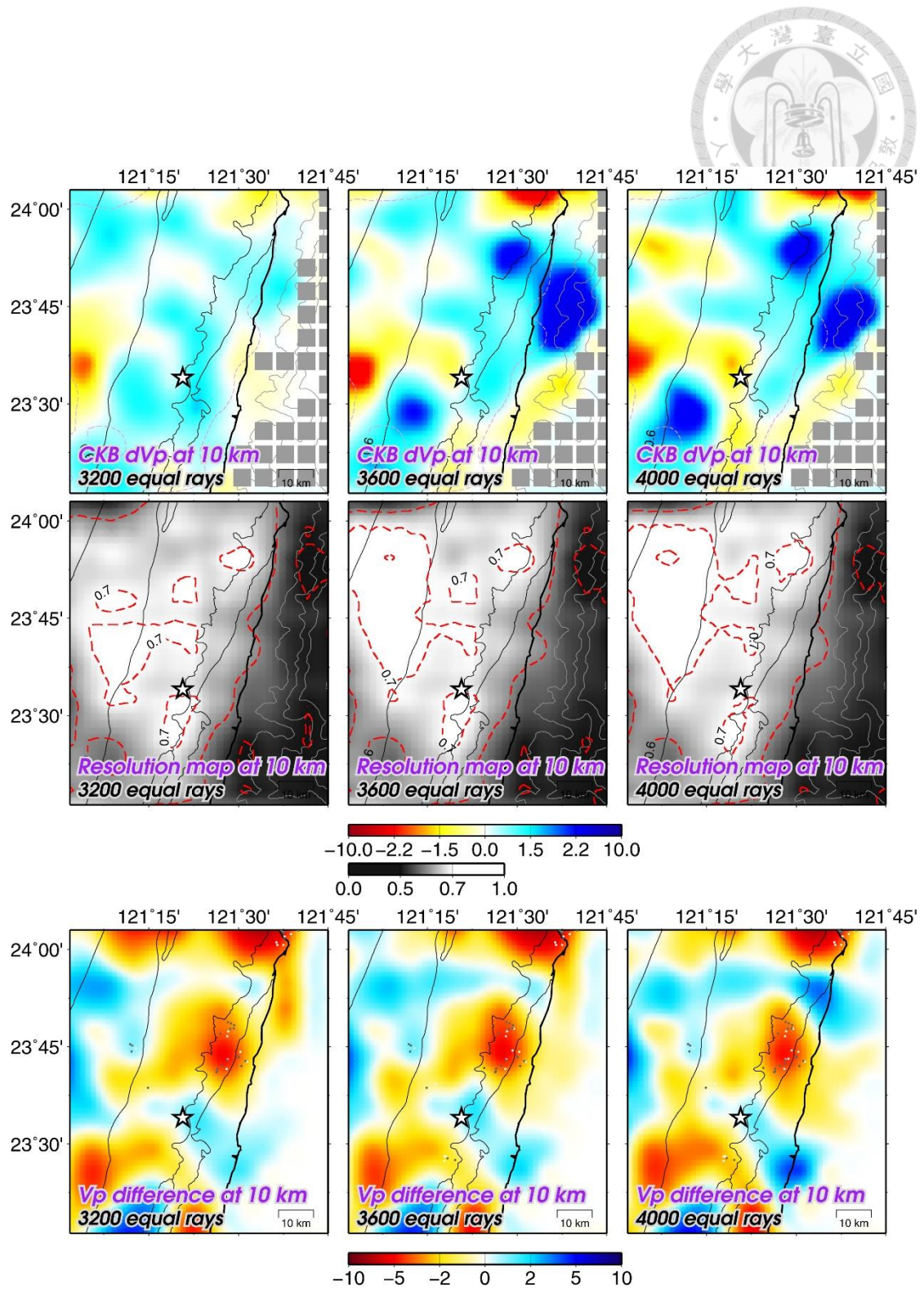


Figure C 1. Discrepancy of checkerboard-like structures, resolution maps and ΔM in V_P at 10 km depth considering an initial 3-D velocity model the equal-type travel time data (3200, 3600 and 4000-arrivals), and no station corrections between two time periods.

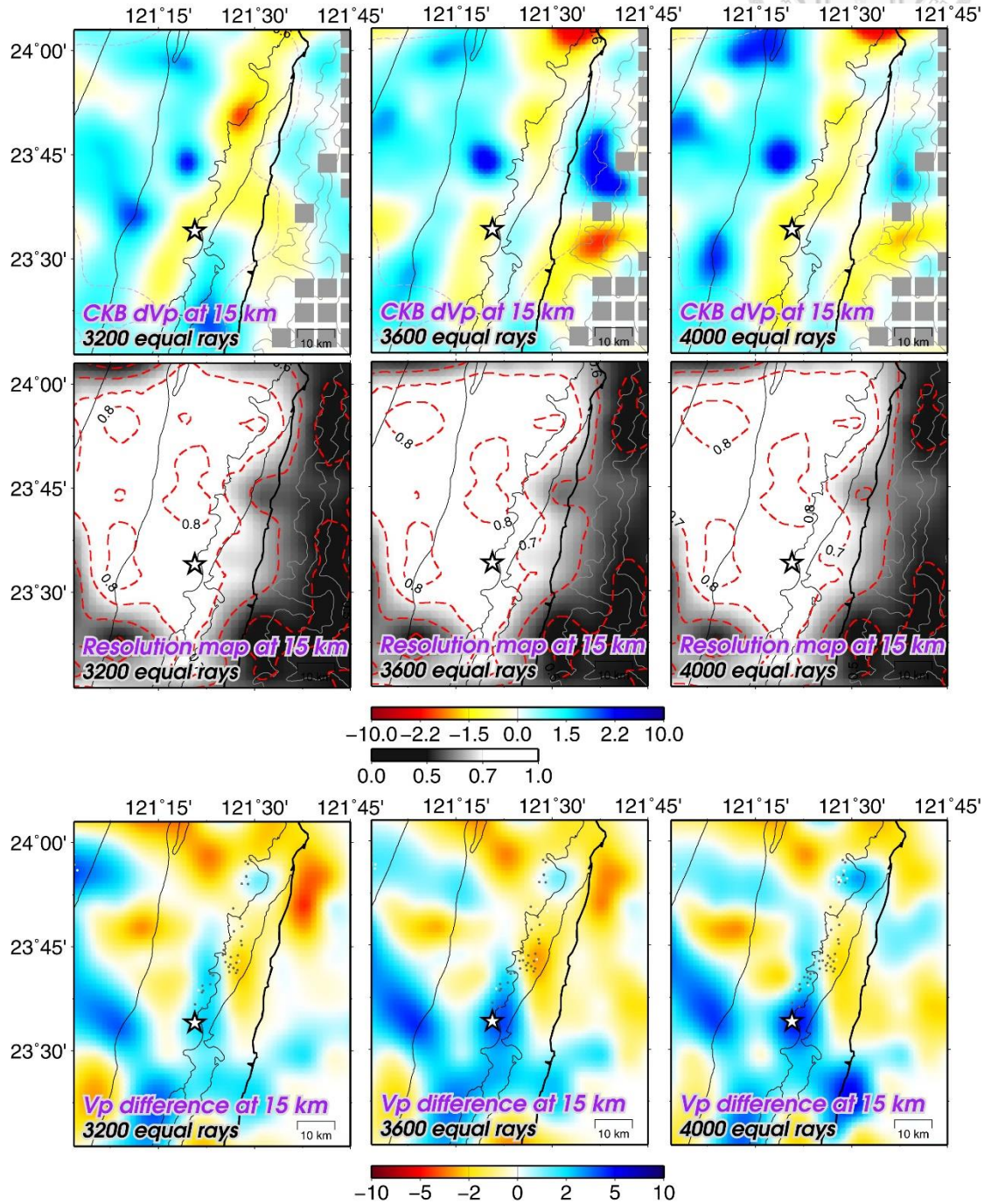


Figure C 2. Discrepancy of checkerboard-like structures, resolution maps and ΔM in V_P at 15 km depth considering an initial 3-D velocity model the equal-type travel time data (3200, 3600 and 4000-arrivals), and no station corrections between two time periods.

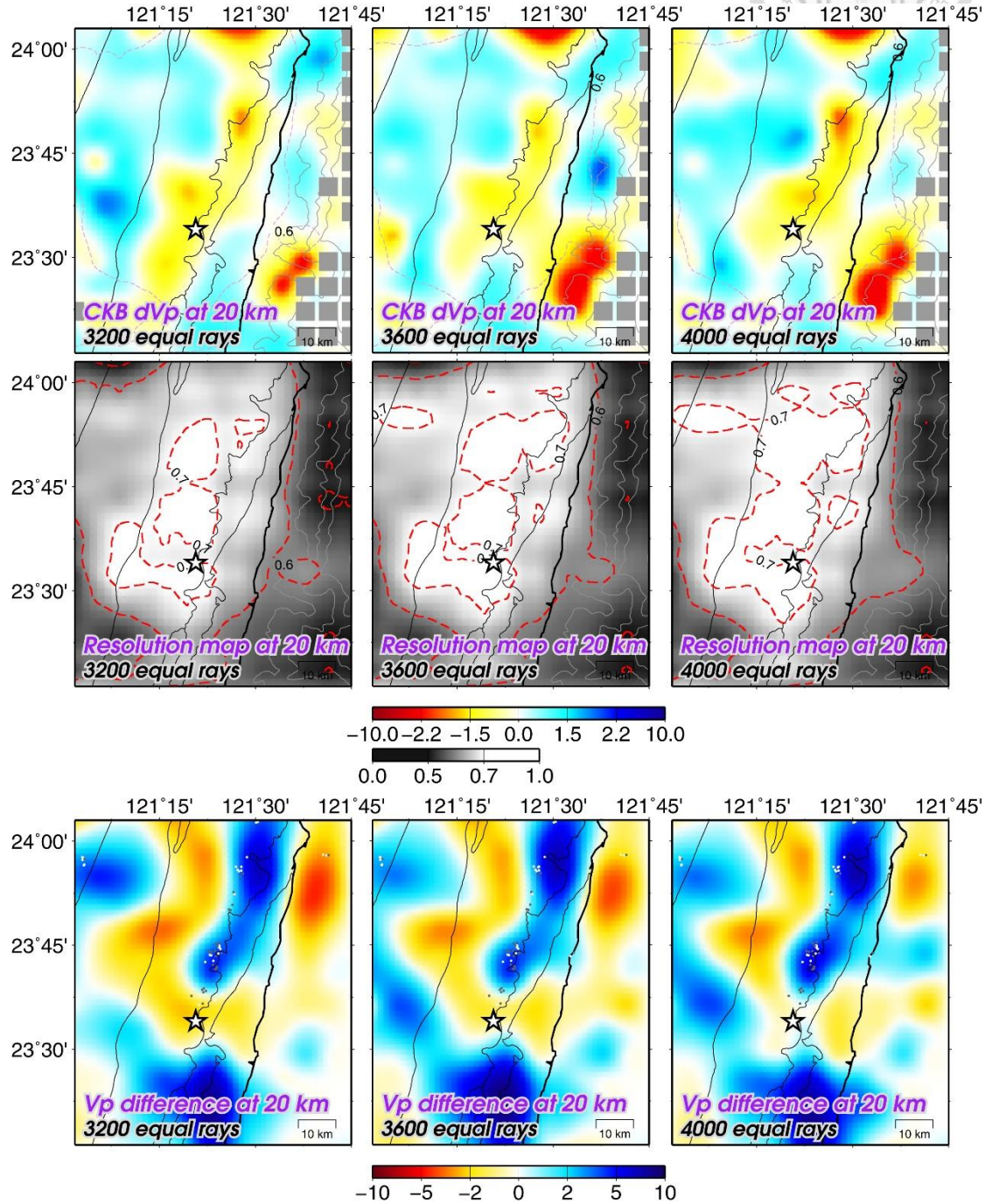


Figure C 3. Discrepancy of checkerboard-like structures, resolution maps and ΔM in V_P at 20 km depth considering an initial 3-D velocity model the equal-type travel time data (3200, 3600 and 4000-arrivals), and no station corrections between two time periods.

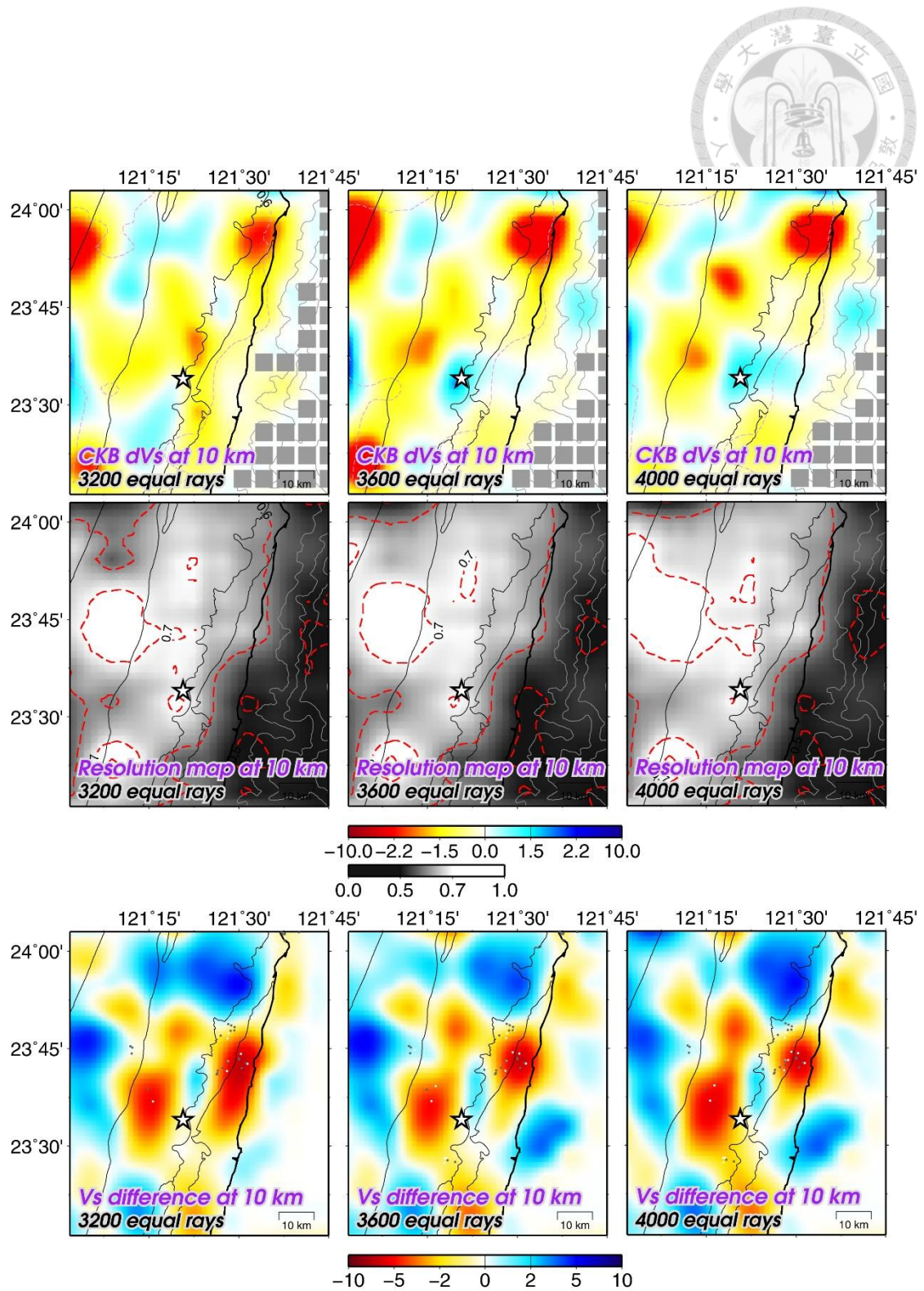


Figure C 4. Discrepancy of checkerboard-like structures, resolution maps and ΔM in V_S at 10 km depth considering an initial 3-D velocity model the equal-type travel time data (3200, 3600 and 4000-arrivals), and no station corrections between two time periods.

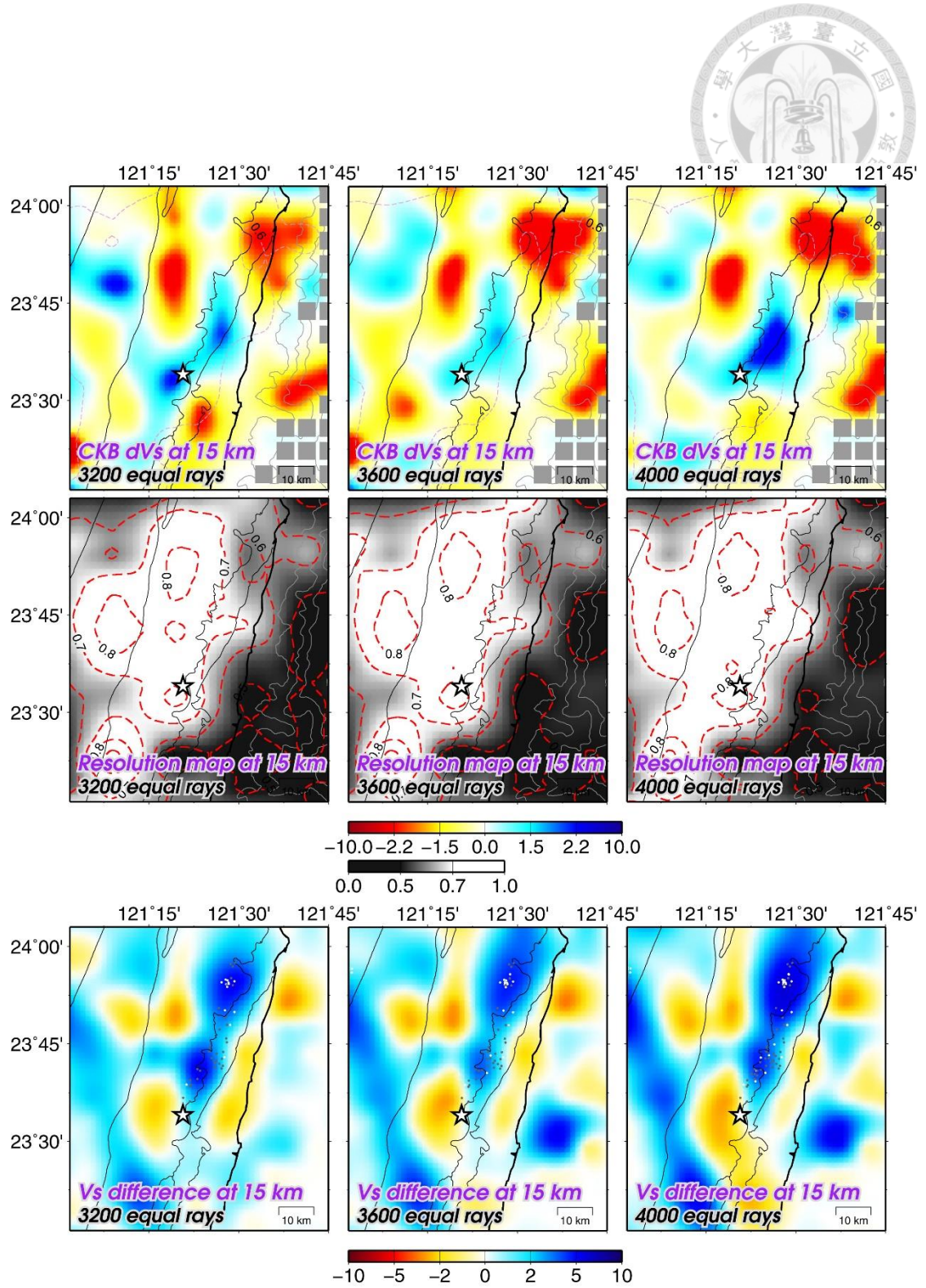


Figure C 5. Discrepancy of checkerboard-like structures, resolution maps and ΔM in V_S at 15 km depth considering an initial 3-D velocity model, the equal-type travel time data (3200, 3600 and 4000-arrivals), and no station corrections between two time periods.

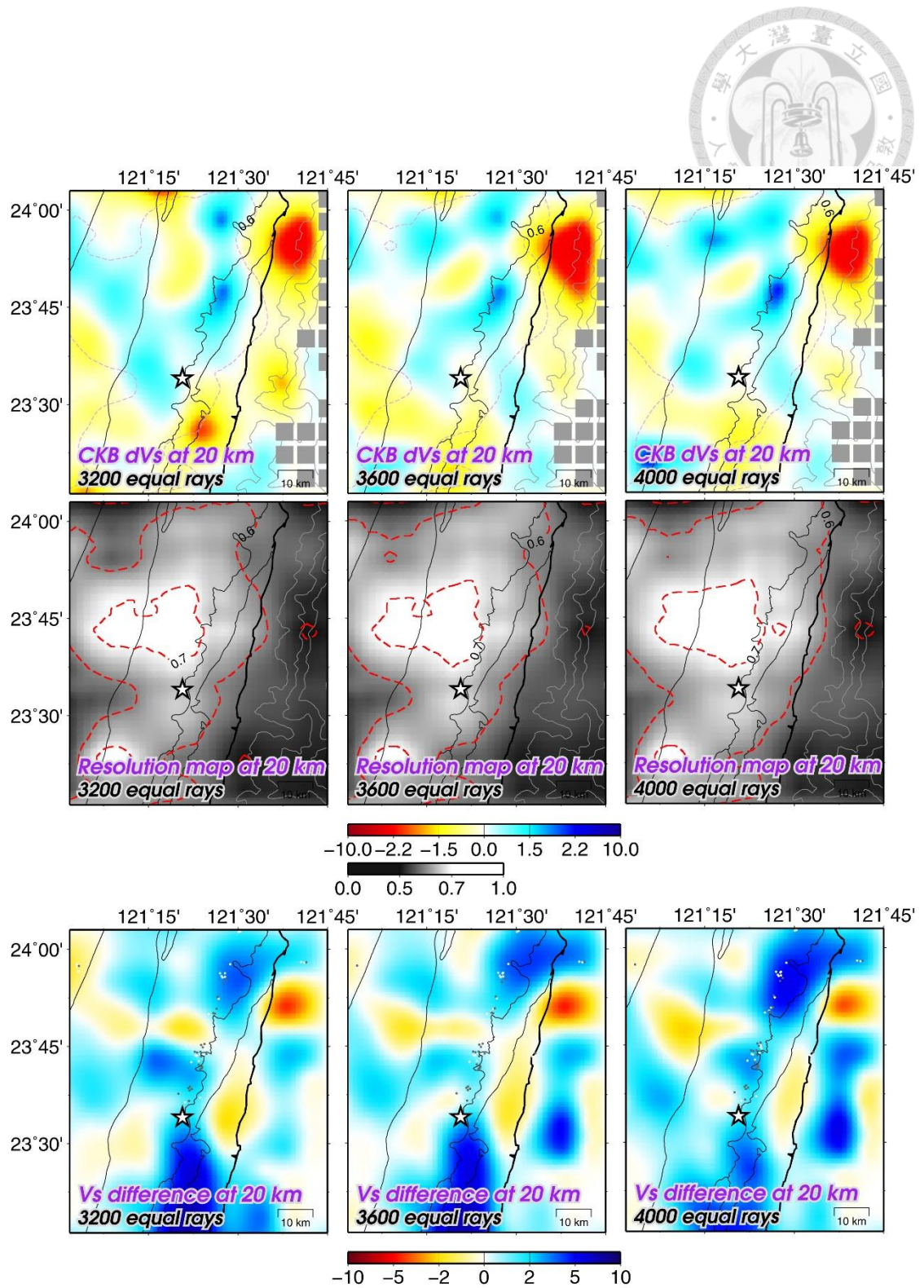


Figure C 6. Discrepancy of checkerboard-like structures, resolution maps and ΔM in V_S at 20 km depth considering an initial 3-D velocity model, the equal-type travel time data (3200, 3600 and 4000-arrivals), and no station corrections between two time periods.

D. Tomographic inversion with an initial 1-D velocity model and equal-type travel time data

Figure D2 shows the ΔM results of equal-type travel time data inverted with an initial 1-D velocity model and the optimal value of damping (λ) and smoothing (φ) factors (Figure D1). Many strong anomalies appeared on the boundary of study area due to lacking of ray coverages (Figure 2.1(b) and (d)). It again demonstrated how initial velocity model and data constrain the inversion.

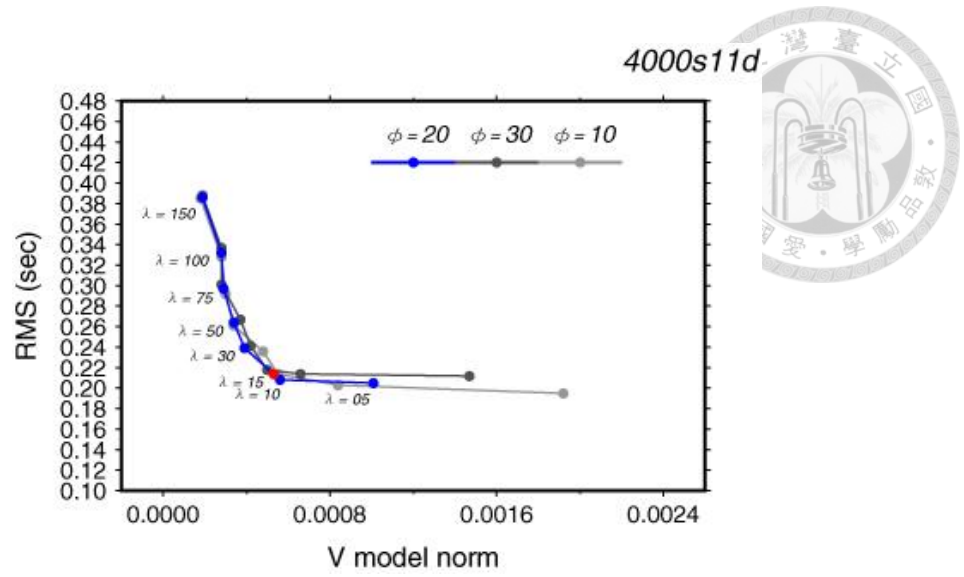


Figure D 1. The trade-off curve test considering the equal-type travel time data and an initial 1-D model.

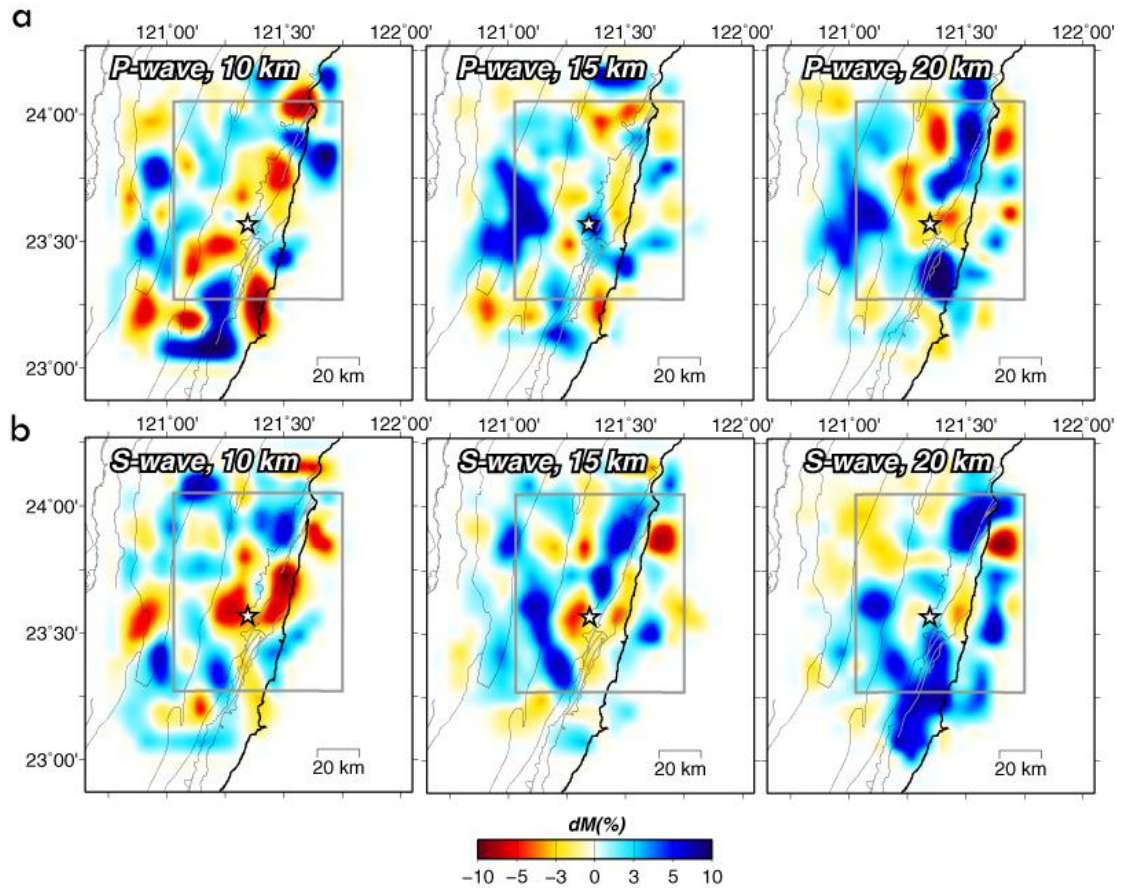
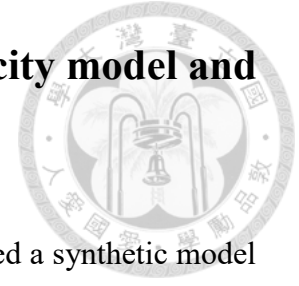


Figure D 2. The results of ΔM considering an initial 1-D model, equal-type travel time data and no station corrections. The value of damping (λ) and smoothing (ϕ) factors were determined from the trade-off curve test (Figure D1) which were chosen to be 15 and 20, respectively.

E. Synthetic test considering an initial 3-D velocity model and equal-type travel time data



In order to test the robustness of obtained results, we constructed a synthetic model with three velocity anomalies according to the initial 3-D model (Figures E1(a) and E2(a)): two negative velocity anomalies ($0.18^\circ \times 0.12^\circ$ in horizontal with 10% in amplitude) and one positive velocity anomaly ($0.30^\circ \times 0.18^\circ$ in horizontal with 8% in amplitude). The negative anomalies in the northeastern and in the southwestern region of the epicenter location had the range of depth from 6 km to 10 km and from 10 km to 15 km, respectively. The positive anomaly had the range of depth from 15 km to 20 km. The equal-type travel time data and the constructed synthetic structure were used to forwardly get the artificial travel times. Further, these artificial travel time data were inverted to recovered the synthetic structure (Figure E1 (a) and Figure E2 (a)).

Figures E1 (b and c) and E2 (b and c) show the results of synthetic test in V_P and V_S for pre-seismic and post-seismic time periods at 10, 15 and 20 km depth, respectively. The shapes of input anomalies were recovered well, especially at depth of 15 and 20 km and the difference of recovery levels in between were quite small, too (Figure E1 (d) and Figure E2 (d)).

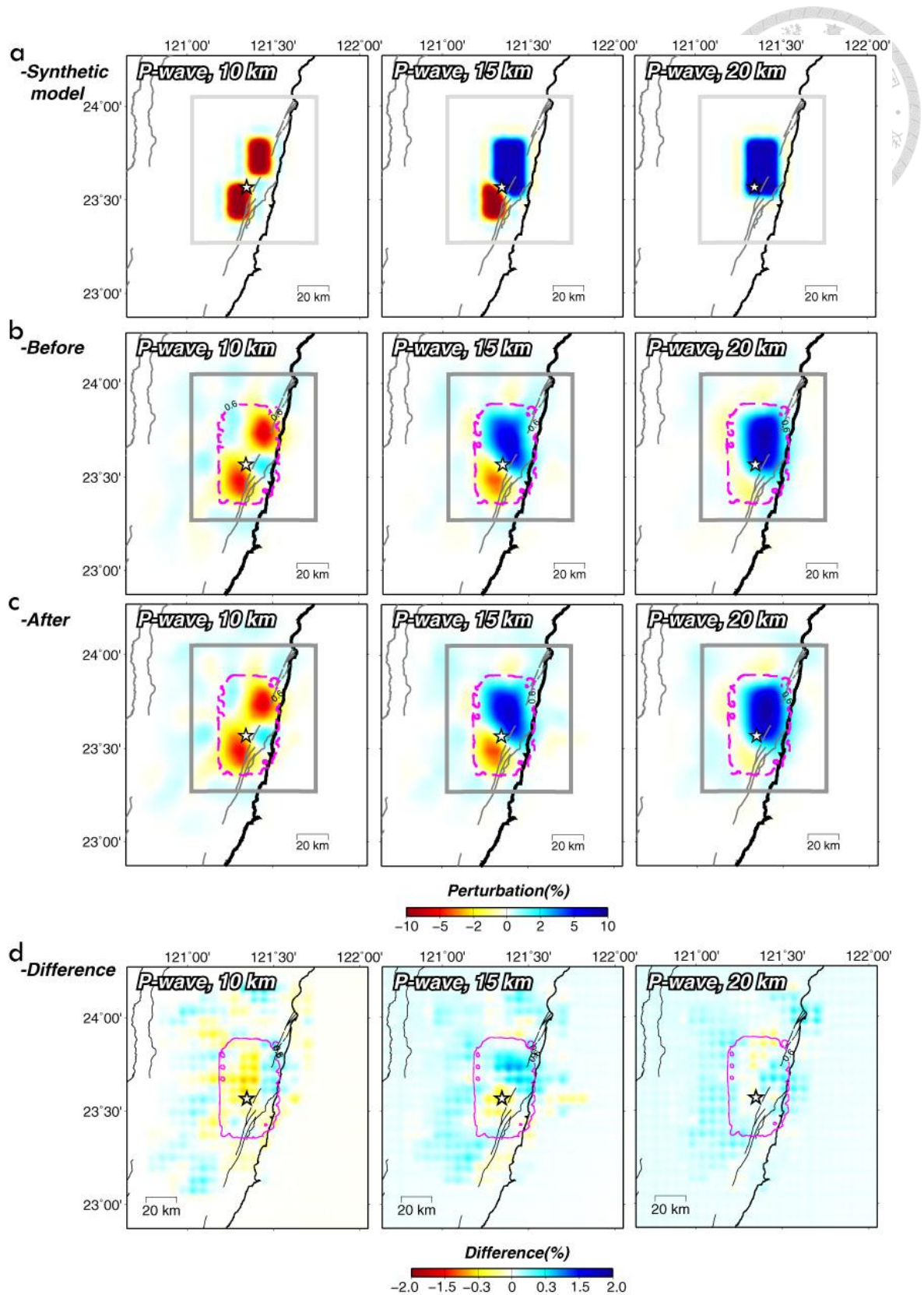


Figure E 1. The results of synthetic test in V_p considering an initial 3-D model, three anomalies and equal-type travel time data with station corrections in 10, 15 and 20 km depth. (a) The constructed synthetic model. (b) The result of pre-seismic periods. (c) The result of post-seismic periods. (d) The difference between (b) and (c).

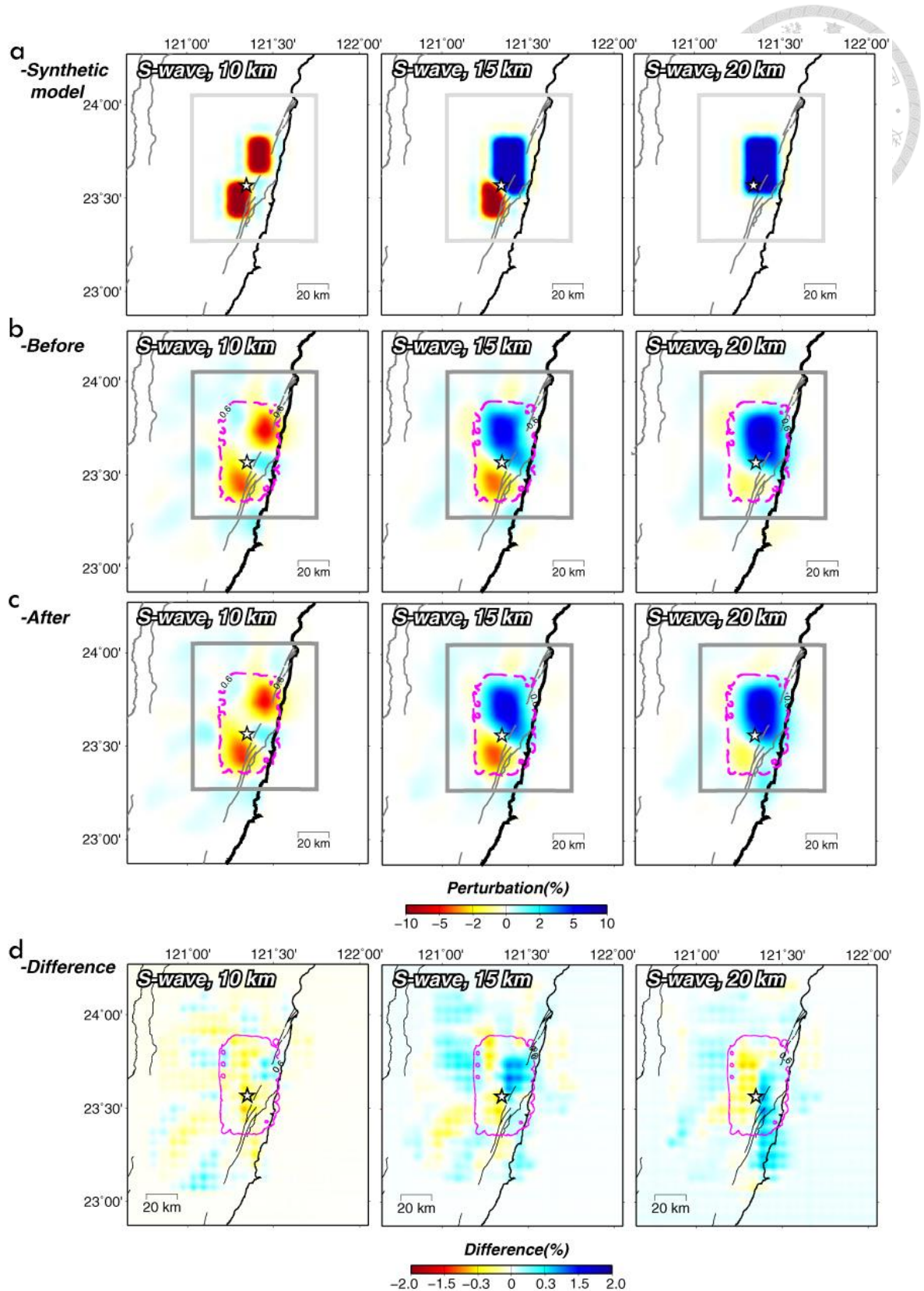



Figure E 2. The results of synthetic test in V_s considering an initial 3-D model, three anomalies and equal-type travel time data with station corrections in 10, 15 and 20 km depth. (a) The constructed synthetic model. (b) The result of pre-seismic periods. (c) The result of post-seismic periods. (d) The difference between (b) and (c).



F. Testing the influence of weighting value of arrival-pickings in travel time data on tomography with the checkerboard-like structure considering an initial 3-D velocity model and equal-type travel time data

Owing to examine the effect of weighting value of arrival-pickings in travel time data to tomography, we performed the checkerboard resolution test considering an initial 3-D velocity model and the equal-type travel time data with station corrections and all travel time data had the same weighting value of arrival-pickings. The checkerboard-like structures both of pre-seismic and post-seismic time periods were retrieved after 15 iterations.

Figures F1 and F2 show the results of dV and R maps in V_P and V_S . Some localized dV in Figures 4.4 and 4.5 disappeared, especially in V_P . Generally, P -wave arrivals are easier to pick than S -wave arrivals so that the more uniform dV distributed in V_P than in V_S . However, in order to check the recovery level distribution of inverted velocity structures, the weighting value referred to real arrival pickings should be considered rather than the same value.

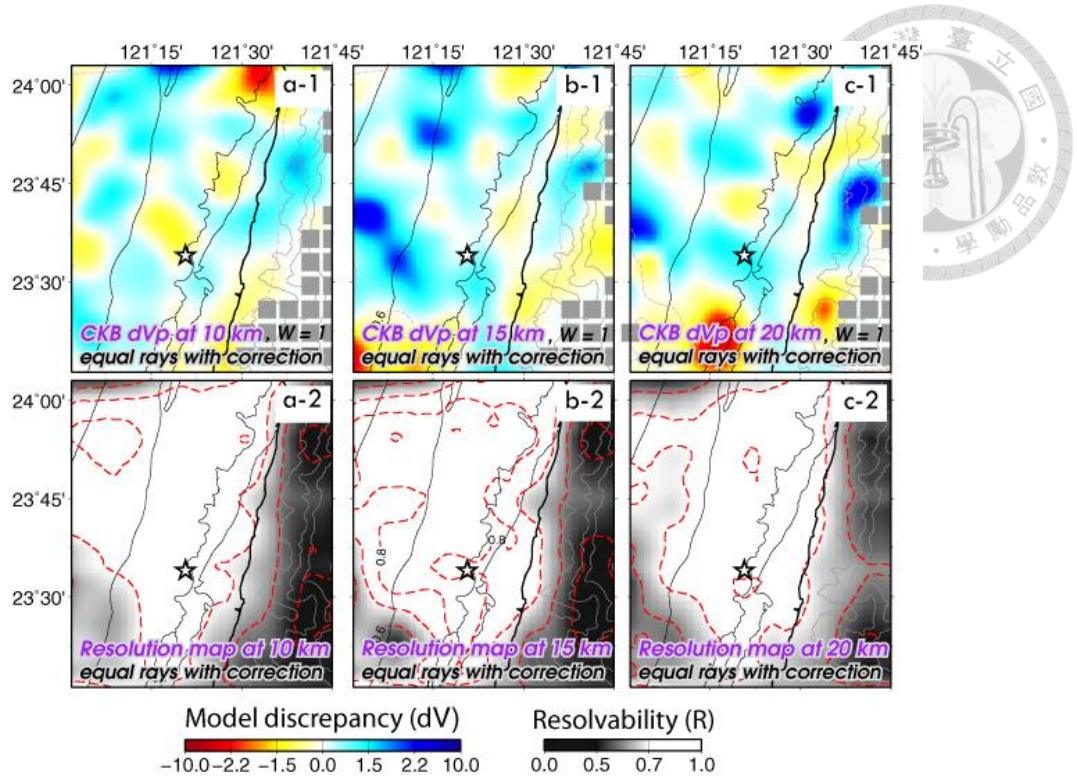


Figure F 1. Discrepancy of checkerboard-like structures, resolution maps in V_P and V_S at 10, 15 and 20 km depth considering an initial 3-D velocity model and the equal-type travel time data with station corrections and the same weighting value between two time periods.

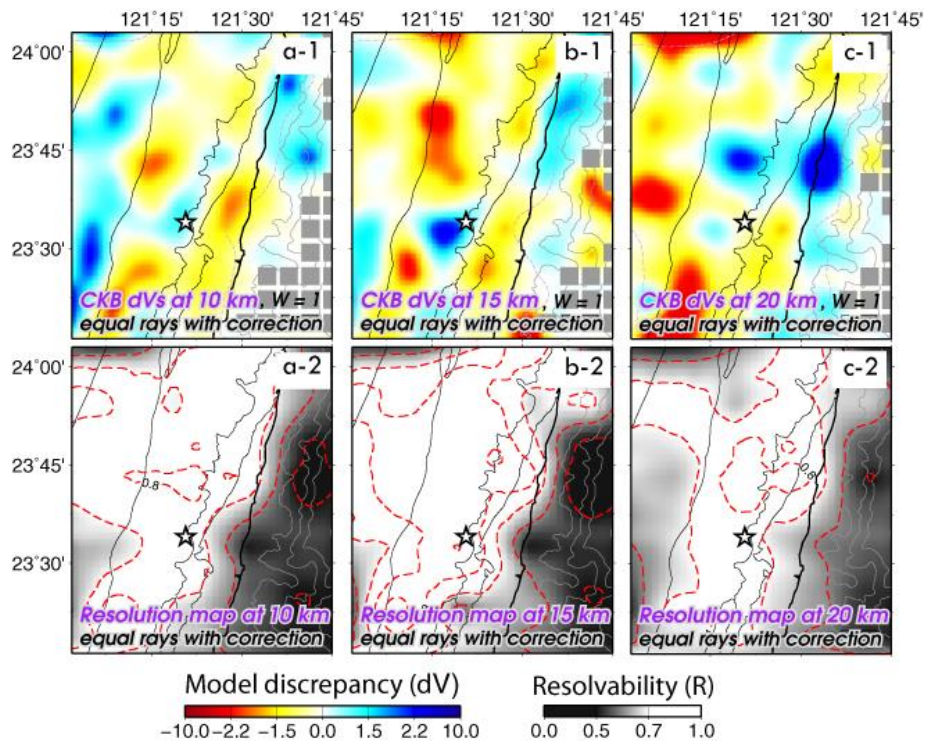


Figure F 2. (Continued.)